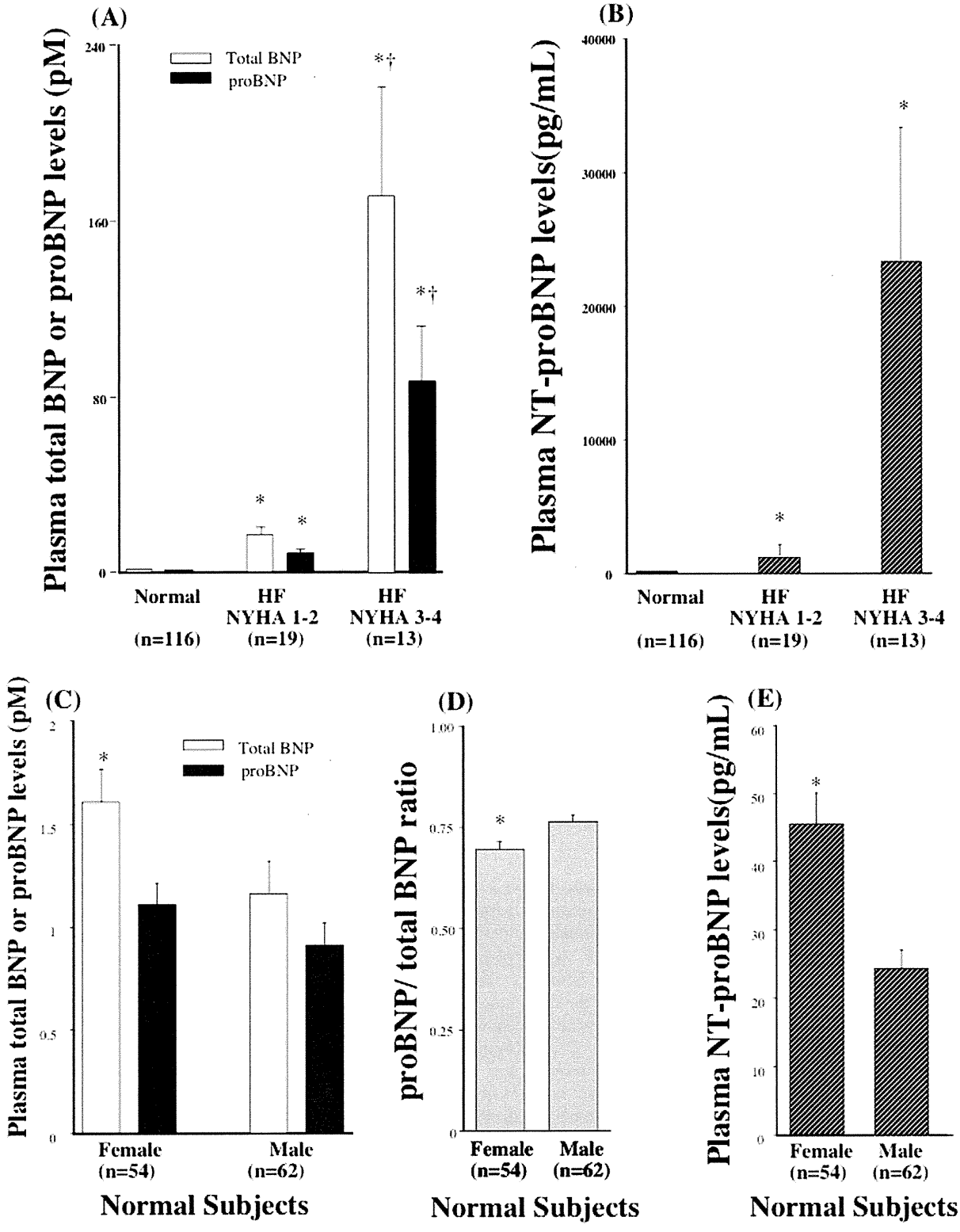

Figure 6. Plasma Levels of proBNP, total BNP, and NT-proBNP in normal and heart failure. Bar graph showing the total BNP, proBNP (A) and NT-proBNP (B) levels in healthy subjects and heart failure patients with NYHA classes 1–2 and 3–4. *P<0.05 vs total BNP and proBNP in normal, †P<0.05 vs total BNP and proBNP in HF NYHA 1–2. Bar graph showing the total BNP, proBNP (C), proBNP/total BNP ratio (D) and NT-proBNP (E) levels in male and female in healthy subjects. Values are means ± SE. *P<0.05 vs male.
doi:10.1371/journal.pone.0053233.g006

and a fluorescent immunoenzyme assay to measure BNP and proBNP, we found that levels of BNP were slightly higher than those of proBNP in both healthy subjects and heart failure patients. The exact reason for the discrepancy in proBNP levels between the earlier study and the present one is unclear; however, the lower recovery caused by the need for extraction from plasma on a Sep-Pak C18 cartridge may have contributed to the lower proBNP levels in the earlier study [9,16]. Recent studies have shown that proBNP has much less ability to induce cGMP production in vascular smooth muscle and endothelial cells than BNP [7,18]. This suggests that increases in the levels of the low-activity proBNP in heart failure may contribute to the so-called "BNP paradox" [19]. That is, administration of exogenous recombinant human BNP to heart failure patients has a substantial clinical and hemodynamic impact, despite the presence of high levels of immunoreactive BNP in their plasma, as measured with commercially used BNP assays.

In the current study, we showed that total BNP and NT-proBNP increased with aging, which are consistent with the previous studies. In addition, the current study first showed that plasma proBNP level increased with aging. However, there were no statistical differences in NT-proBNP between 30~39 and 50~59, whereas there were significant differences in total and proBNP between 30~39 and 50~59, suggesting that total and proBNP are more sensitive than NT-proBNP. In addition, total and proBNP seemed to be well correlated with age ($r = 0.467$. 0.491, each) than NT-proBNP ($r = 0.376$). Thus, total BNP and proBNP may be better marker in discriminating the effect of age than NT-proBNP. Increased myocardial mass and/or reduction of renal clearance of natriuretic peptides with aging may be one of the possible reason for increased BNP and NT-BNP with aging; however, exact mechanism for it still remains unknown and further study is necessary to investigate the relationships between proBNP and aging.

We also analyzed the effects of gender on proBNP, total BNP, proBNP/total BNP ratio and NT-proBNP. Interestingly, in female higher total BNP and NT-proBNP and lower proBNP/total BNP ratio without changing of proBNP was observed. Calculated BNP (total BNP - proBNP) was also increased. This finding may be explained that increased proBNP production and higher processing rate. Further study is necessary to elucidate the mechanism of increased total BNP and NT-proBNP and lower proBNP/total BNP ratio without changing of proBNP in female.

In summary, we have developed rapid and precise immunochemiluminescent assay systems for routine determination of total BNP and proBNP levels in human plasma. Using these assay systems we showed that in addition to BNP, considerable amount of proBNP circulates in both healthy subjects and heart failure patients. The precise relation of the proBNP/total BNP ratio to heart failure remains unknown, as does whether the heart mainly secretes proBNP. Likewise, the effects of age, sex and renal function on proBNP levels remain unknown. We anticipate our new assays for the proBNP and total BNP will be helpful for addressing each of those issues.

Acknowledgments

We thank Ms. Aoi Fujishima and Masako Matsubara for her excellent technical assistance and Ms.Yukari Kubo for her excellent secretarial work.

Author Contributions

Gave useful comments and discussion: K. Kamgawa K. Nakao. Conceived and designed the experiments: TN HO NM KH. Performed the experiments: MN NO K. Nagata. Analyzed the data: YN HK CY K. Nakao. Contributed reagents/materials/analysis tools: TM YK K. Koichiro IM. Wrote the paper: TN HO.

References

1. Maisel AS, Nakao K, Ponikowski P, Peacock WF, Yoshimura M, et al. (2011) Japanese-Western consensus meeting on biomarkers. Int Heart J. 52:253–65.
2. Jessup M, Abraham WT, Casey DE, Feldman AM, Francis GS, et al. (2009) ACCF/AHA Guidelines for the Diagnosis and Management of Heart Failure in Adults: a report of the American College of Cardiology Foundation/American Heart Association Task Force on Practice Guidelines: developed in collaboration with the International Society for Heart and Lung Transplantation. Circulation. 119:1977–2016.
3. Dickstein K, Cohen-Solal A, Filippatos G, McMurray JJ, Ponikowski P, et al. (2008) ESC Guidelines for the diagnosis and treatment of acute and chronic heart failure 2008: the Task Force for the Diagnosis and Treatment of Acute and Chronic Heart Failure 2008 of the European Society of Cardiology. Developed in collaboration with the Heart Failure Association of the ESC (HFA) and endorsed by the European Society of Intensive Care Medicine (ESICM). ESC Committee for Practice Guidelines (CPG). Eur Heart J. 29:2388–442.
4. Minamino N, Horio H, Nishikimi T (2006) Chapter 165. Natriuretic peptides in the cardiovascular system. In: Kastin AJ, editor. THE HANDBOOK OF BIOLOGICALLY ACTIVE PEPTIDES. 1st ed. Academic Press, pp. 1217–1225
5. Waldo SW, Beede J, Isakson S, Villard-Saussine S, Farch J, et al. (2008) Pro-B-type natriuretic peptide levels in acute decompensated heart failure. J Am Coll Cardiol. 51:1874–82.
6. Nishikimi T, Minamino N, Ikeda M, Takeda Y, Tadokoro K, et al. (2010) Diversity of molecular forms of plasma brain natriuretic peptide in heart failure–different proBNP-108 to BNP-32 ratios in atrial and ventricular overload. Heart. 96:432–9.
7. Liang F, O'Rear J, Schellenberger U, Tai L, Lasecki M, et al. (2007) Evidence for functional heterogeneity of circulating B-type natriuretic peptide. J Am Coll Cardiol. 49:1071–8.
8. Nishikimi T, Minamino N, Horii K, Matsuoka H (2007) Do commercially available assay kits for B-type natriuretic peptide measure Pro-BNP1-108, as well as BNP1-32? Hypertension. 50:e163
9. Semenov AG, Seferian KR (2011) Biochemistry of the human B-type natriuretic peptide precursor and molecular aspects of its processing. Clin Chim Acta. 412:850–60
10. Tsuji T, Inouye K, Yamauchi A, Kono M, Igano K (2004) U.S. Patent 6, 677, 124 B2, pp 16, Shionogi Seiyaku Kabushiki Kaisha, Japan.
11. Seferian KR, Tamm NN, Semenov AG, Tolstaya AA, Koshkina EV, et al. (2008) Immunodetection of glycosylated NT-proBNP circulating in human blood. Clin Chem. 54:866–73.
12. Ishikawa E, Imagawa M, Hashida S, Yoshitake S, Hamaguchi Y, et al. (1983) Enzyme-labeling of antibodies and their fragments for enzyme immunoassay and immunohistochemical staining. J Immunoassay. 4:209–327.
13. Nishikimi T, Ikeda M, Takeda Y, Ishimitsu T, Shibasaki I, et al. (2012) The effect of glycosylation on plasma N-terminal proBNP-76 levels in patients with heart or renal failure. Heart. 98:152–61
14. Schellenberger U, O'Rear J, Guzzetta A, Jue RA, Protter AA, et al. (2006) The precursor to B-type natriuretic peptide is an O-linked glycoprotein. Arch Biochem Biophys. 451:160–6.
15. Nishikimi T, Kuwahara K, Nakao K. (2011) Current biochemistry, molecular biology, and clinical relevance of natriuretic peptides. J Cardiol. 57:131–40.
16. Seferian KR, Tamm NN, Semenov AG, Mukharyamova KS, Tolstaya AAet al. (2007) The brain natriuretic peptide (BNP) precursor is the major immunoreactive form of BNP in patients with heart failure. Clin Chem. 53:866–73.
17. Hammerer-Lercher A, Halfinger B, Sarg B, Mair J, Puschendorf B, et al. (2008) Analysis of circulating forms of proBNP and NT-proBNP in patients with severe heart failure. Clin Chem. 54:858–65.
18. Heublein DM, Huntley BK, Boerrigter G, Cataliotti A, Sandberg SM, et al. (2007) Immunoreactivity and guanosine 3′,5′-cyclic monophosphate activating actions of various molecular forms of human B-type natriuretic peptide. Hypertension. 49:1114–9.
19. Menon SG, Mills RM, Schellenberger U, Saqhir S, Protter AA (2009) Clinical implications of defective B-type natriuretic peptide. Clin Cardiol. 32:E36–41.

Cerebral Cortex Advance Access published June 1, 2012

Cerebral Cortex
doi:10.1093/cercor/bhs141

Robo1 Regulates the Migration and Laminar Distribution of Upper-Layer Pyramidal Neurons of the Cerebral Cortex

Yuko Gonda[1,2], William D. Andrews[3], Hidenori Tabata[4], Takashi Namba[2], John G. Parnavelas[3], Kazunori Nakajima[4], Shinichi Kohsaka[2], Carina Hanashima[1] and Shigeo Uchino[2]

[1]Laboratory for Neocortical Development, RIKEN Center for Developmental Biology, Kobe 650-0047, Japan [2]Department of Neurochemistry, National Institute of Neuroscience, Kodaira-shi, Tokyo 187-8502, Japan [3]Department of Cell and Developmental Biology, University College London, London WC1E 6BT, UK [4]Department of Anatomy, School of Medicine, Keio University, Tokyo 160-8582, Japan

Address correspondence to C. Hanashima, Laboratory for Neocortical Development, RIKEN Center for Developmental Biology, 2-2-3 Minatojima-minamimachi, Chuo-ku, Kobe 650-0047, Japan. Email: hanashima@cdb.riken.jp.

Laminar organization is a key feature of the mammalian cerebral cortex, but the mechanisms by which final positioning and "inside-out" distribution of neurons are determined remain largely unknown. Here, we demonstrate that Robo1, a member of the family of Roundabout receptors, regulates the correct positioning of layers II/III pyramidal neurons in the neocortex. Specifically, we used RNA interference in mice to suppress the expression of *Robo1* in a subset of layers II/III neurons, and observed the positions of these cells at distinct developmental stages. In contrast to control neurons that migrated toward the pial surface by P1, *Robo1*-suppressed neurons exhibited a delay in entering the cortical plate at respective stages. Unexpectedly, after the first postnatal week, these neurons were predominantly located in the upper part of layers II/III, in contrast to control cells that were distributed throughout these layers. Sequential electroporation studies revealed that *Robo1*-suppressed cells failed to establish the characteristic inside-out neuronal distribution and, instead, they accumulated beneath the marginal zone regardless of their birthdate. These results demonstrate that Robo receptors play a crucial role in neocortical lamination and particularly in the positioning of layers II/III pyramidal neurons.

Keywords: lamination, layers II/III, neocortex, neuronal positioning, Roundabout

Introduction

The mammalian cerebral cortex consists of 6 distinct layers that are largely represented by its excitatory neurons with characteristic axon projection patterns and gene expressions. Early in corticogenesis, neurons arise from the ventricular (VZ) and subventricular (SVZ) zones and move radially toward the pial surface (Pearlman et al. 1998; Nadarajah et al. 2001). Subsequent cohorts of later-born neurons migrate past their predecessors to take a more superficial position within the cortical plate (CP), resulting in an "inside-out" neuronal distribution pattern (Angevine and Sidman 1961; Rakic 1974). It is considered that the latter process involves a series of migration and positioning events such as multipolar-to-bipolar transition of neurons (Tabata and Nakajima 2003; Noctor et al. 2004; Tabata et al. 2009), radial glia-guided locomotion (Rakic 1972; O'Rourke et al. 1992; Nadarajah et al. 2001), detachment from radial glial fibers (Pinto-Lord et al. 1982; Gongidi et al. 2004; Elias et al. 2007), and terminal somal translocation (Nadarajah et al. 2001; Borrell et al. 2006; Sekine et al. 2011). The complex behavior of neurons during radial migration suggests that distinct molecular mechanisms may regulate each of the migration steps during development. Indeed, an increasing number of genes have been identified that control the early phase of radial migration (Caviness and Rakic 1978; Gupta et al. 2002; Nadarajah and Parnavelas 2002; Tsai and Gleeson 2005; Cooper 2008; Huang 2009; Honda et al. 2011). In contrast, much less is known about how the terminal positioning of neurons is regulated after they arrive at the surface of the CP. Although it has long been postulated that inside-out neuronal distribution requires a correct termination of radial migration through the local interaction between extracellular glycoprotein Reelin and its receptors (Dulabon et al. 2000; Sanada et al. 2004), confirmation of such pathway using transgenic mouse models has remained elusive (Magdaleno et al. 2002; Yoshida et al. 2006). Alternative signaling pathways may contribute to this process (Moers et al. 2008), but the positioning defects appear only in a limited number of neurons. This prompted us to investigate whether additional mechanisms may contribute to the correct positioning of the cortical neurons after they reach the upper part of the CP.

Roundabout (Robo) was first identified as a receptor for the chemorepulsive ligand Slit in the *Drosophila* nerve cord (Kidd, Brose et al. 1998). In the mammalian spinal cord and *Drosophila* nerve cord, Robo proteins play a crucial role in preventing the commissural axons from re-crossing the midline through growth cone repulsion (Kidd, Brose et al. 1998; Kidd, Russell et al. 1998; Chen et al. 2008). In the mammalian forebrain, Robo signaling has also been shown to play key roles in the axonal pathfinding (Andrews et al. 2006, 2008; López-Bendito et al. 2007). Furthermore, recent studies have shown that the inhibition of Robo1-mediated signaling can affect the proliferation and migration of the neocortical interneurons (Andrews et al. 2006, 2008; Hernandez-Miranda et al. 2011). These findings support the notion that Robo receptors may play an important role beyond axonal pathfinding in the developing neocortex.

In this study, we examined the cortical neuron subtypes that express Robo1 during development. We found that *Robo1* mRNA and Robo1 protein are expressed in pyramidal neurons as they enter the CP, and in restricted zones including the upper part of layers II/III. To investigate the role of this receptor in the development of upper-layer projection neurons in vivo, we suppressed *Robo1* expression in pyramidal neurons of layers II/III using RNA interference. Here, we report that *Robo1*-suppressed neurons exhibit a delay in entering the CP during the embryonic period. Moreover,

although these neurons eventually migrate to the pial surface by the middle of the first postnatal week, they are predominantly located in the uppermost part of layers II/III after the first postnatal week. Sequential in utero electroporation of *Robo1*-shRNA constructs at E15.5 and E16.5 in the same cortices revealed that *Robo1*-suppressed cells fail to establish the typical inside-out distribution and accumulate beneath the marginal zone (MZ) regardless of their birthdates. These differences were not observed in E14.5 *Robo1*-shRNA-transfected neurons. Our results indicate that Robo1 is a key regulatory molecule that controls the laminar distribution and migration of layers II/III pyramidal neurons in the neocortex.

Materials and Methods

Animals

Pregnant Institute of Cancer Research (ICR) mice were purchased from CLEA Japan, Inc. The day the vaginal plug was detected was designated as E0.5. *Robo1*$^{-/-}$ knockout mice were generated by intercrossing *Robo1*$^{+/-}$ heterozygote mice as described previously (Andrews et al. 2008). All animal experiments were performed in accordance with The Animal Care and Use Committee of the National Institute of Neuroscience, RIKEN, and UCL ethics guidelines. Animals of either sex were used in our experiments.

In Situ Hybridization

Complementary DNA (cDNA) of mouse *Robo1* (GenBank accession number AK040651) which had been cloned into the pFLCI vector was used to make the cRNA probe. The cDNA fragment of the unique region of *Robo1* (770 bp) was obtained by PCR using the following primers: Robo1-F (5′-GGGGAATTCAATGAGTTTCAAGGAGCA-3′), Robo1-R (5′-CCCAAGCTTGCGACTGTAGGTTGTCAG-3′), annealing temperature 61°C, and subcloned into the mammalian expression vector pCMV-SPORT (Gibco BRL). Digoxigenin (DIG)-labeled antisense and sense cRNA probes were produced with T7 and SP6 polymerase, respectively, using in vitro transcription according to the manufacturer's instructions (Roche Diagnostics).

The in situ hybridization analysis was performed as described previously (Gonda et al. 2007), with a slight modification. Briefly, the brains were fixed with 4% paraformaldehyde (PFA), coronally sliced into 14 μm sections using a Cryostat (CM-3000; Leica), and mounted onto Matsunami adhesive silane (MAS)-coated glass slides (Matsunami). Hybridization of the DIG-labeled cRNA probes (1 μg/mL) on brain sections was performed at 60°C overnight, and was followed by washing twice with 50% formamide, 0.2% saline sodium citrate at 60° C for 30 min each, and once with maleic acid buffer containing 0.2% Tween 20 at room temperature for 3 min. Incubation of alkaline phosphatase-conjugated anti-DIG antibody (1:2000, Roche Diagnostics) was performed at 4°C overnight, and sections were visualized with 0.4 mM nitro blue tetrazolium and 0.35 mM 5-bromo-4-chrolo-3-indoylphosphate at room temperature overnight. The reaction was stopped by rinsing in water twice at room temperature for 5 min each, and sections were dehydrated using a graded ethanol series (70%, 80%, 90%, 95%, and 100%) for 1 min each, and cleared 3 times in xylene for 5 min each. The sections were finally mounted with Entellan (Merck).

Immunohistochemistry

Immunohistochemistry was performed using a floating method as described previously (Namba et al. 2009). Frozen brains fixed with 4% PFA were coronally sliced at 50 μm using a Cryostat (CM-3000), except for Robo1/Satb2 double immunohistochemistry in which sections sliced at 14 μm were used. The following primary antibodies were used: goat polyclonal anti-Robo1 (1:50; R&D System, Inc.), mouse monoclonal anti-Satb2 (1:50; Abcam), rabbit polyclonal anti-Cux1 (1:100; Santa Cruz), rabbit polyclonal anti-enhanced green fluorescent protein (EGFP) (1:1000; Invitrogen), rat monoclonal anti-EGFP (1:500; Nacalai Tesque Inc.), rabbit anti-Calbindin (1:1000; Swant), goat polyclonal anti-Brn2 (1:200; Santa Cruz Biotechnology), mouse monoclonal anti-NeuN (1:500; Chemicon), and mouse monoclonal anti-GFAP (1:1000; Sigma). For detection of goat polyclonal anti-Robo1 antibodies, sections were incubated with biotinylated donkey anti-goat antibody (1:100; Jackson ImmunoResearch Laboratories) for 2 h and processed with a conventional immunohistochemistry protocol using the tyramide signal amplification biotin system (PerkinElmer, Inc.).

For 5-ethynylil-2′-deoxyuridine (EdU) and EGFP double detection, sections were incubated overnight with anti-rabbit EGFP antibody at 4°C and subsequently processed for EdU detection using Click-iT™ EdU Imaging Kit (Invitrogen). Immunostained sections were mounted on MAS-coated glass slides and examined with a confocal laser-scanning microscope (FV1000; Olympus).

Quantification of Neuronal Density and Cortical Layer Thickness

For quantification of neuronal cell density and layers II/III thickness, serial sections (14 μm) were cut from brains of P34-P58 *Robo1*$^{-/-}$ mice and *Robo1*$^{+/+}$ control littermates ($n = 3$). Sections were stained with Cux1 and 4′,6-diamidino-2-phenylindole (DAPI), and matching sections were photographed. All measurements and cell counts were performed on the primary somatosensory cortex (S1 barrel field). For cell density, layers II/III were divided into 6 equal bins according to their mean position in the *Robo1*$^{+/+}$ neocortex and the number of Cux1/DAPI double-positive cells in each bin was counted. The same bin was applied to the *Robo1*$^{-/-}$ cortex; however, due to the decrease in the thickness of layers II/III in the *Robo1*$^{-/-}$ cortex, bin 6 includes Cux1/DAPI double-positive cells of layer IV in the *Robo1*$^{-/-}$ cortex. Total number of Cux1-positive cells in layers II/III was counted per 600 μm width of the *Robo1*$^{-/-}$ and *Robo1*$^{+/+}$ cortices.

Plasmid Construction

For plasmid-based RNA inhibition of *Robo1*, the complementary oligonucleotides for the following target sequence (*Robo1*-shRNA1: 5′-ACTCAAACCTAACGCCA-TTTA-3′; *Robo1*-shRNA2: 5′-AGCTGATTG TATAGCCAATTA-3′; *Robo1*-shRNA3: 5′-TCTCGGTAATGAAACGAAG TA-3′; *Robo1*-shRNA4: 5′-TCCGCTACTTTGAC-AGTTCAA-3′; and Mt-Robo1-shRNA: 5′-ACTCAAACCATTCGCCATTTA-3′) were annealed and inserted into the BamHI/HindIII sites of pSilencer 3.0-H1 (Ambion). As a control plasmid, pSilencer 3.0-H1 Negative Control (Ambion) was used. To construct the *Robo1*-expression vector, full-length cDNA of mouse *Robo1* was inserted into the mammalian expression vector pCAGGS, which contains a modified chicken β-actin promoter with a cytomegalovirus-immediate early enhancer (CAG) promoter (Niwa et al. 1991), provided by Dr J. Miyazaki (Osaka University).

Cell Lines and Western Blot Analysis

COS7 cells were grown at 37°C in a humidified 5% CO_2 atmosphere in the Dulbecco's modified Eagle's medium (Gibco BRL) containing 10% heat-inactivated fetal bovine serum (Irvine Scientific). For transient expression studies, cells were transfected with plasmid DNA using Lipofectamine Plus (Invitrogen) according to the manufacturer's protocol.

COS7 cells or brain tissues were homogenized in lysis buffer (10 mM Tris–HCl [pH 7.4], 150 mM NaCl, 1 mM ethylene diamine tetraacetic acid, 1% Triton X-100, 0.1% sodium deoxycholate, 0.1% sodium dodecyl sulfate, and protease inhibitor cocktail [Roche Diagnostics]) and incubated at 4°C for 1 h. After removing the nuclei and debris by centrifugation (2000 × *g* for 10 min at 4°C), protein concentration of the supernatant was determined using the Bio-Rad Protein Assay Kit (Bio-Rad). Protein samples were subjected to immunoblotting with rabbit polyclonal anti-Robo1 antibody (1:1000; Rockland Immunochemicals) or goat polyclonal anti-Robo2 antibody (1:1000; R&D Systems). Blots were developed with ECL Reagent (GE Healthcare).

In Utero Electroporation

In utero electroporation was performed as previously described (Tabata and Nakajima 2001), with a slight modification. Briefly, timed-pregnant ICR mice were deeply anesthetized with sodium pentobarbitone (Somnopentyl; Kyoritsu Pharmaceuticals), and their uterine horns were exposed. Approximately 1–2 μL of plasmid DNA solution dissolved to a final concentration of 5 mg/mL in 4-(2-hydroxyethyl)-1-piperazineethanesulfonic acid-buffered saline was injected into a lateral ventricle of each embryo with a glass micropipette, and electric pulses (30 V, 50 ms) were discharged 4 times at intervals of 950 ms with an electroporator (CUY21E; Nepa Gene). The uterine horns were then replaced in the abdominal cavity to allow the embryos to continue normal development. For sequential in utero electroporation, plasmids were electroporated into the same cortex at E15.5 and E16.5 with an interval of 24 h.

Fluorescent Activated Cell Sorting

Postnatal (P) day 1 mice transfected with EGFP-expression vector were placed on ice for anesthesia, their brains removed, and EGFP-positive regions were dissected. The dissected tissues were incubated with Liberase Blendzyme I (100 μg/mL; Roche Diagnostics) and DNase I (0.05 mg/mL; Roche Diagnostics) for 15 min at 37°C. The cells were filtered through a 40 μm nylon mesh, and incubated with propidium iodide (Becton Dickinson) (50 μg/mL in phosphate-buffered saline). Sorting and analysis were performed using a FACS Aria flow cytometer (Becton Dickinson). To isolate EGFP-positive cells, physical parameters such as the forward scatter, representing cell size, and the side scatter, representing cellular granularity, and EGFP signals detected with FITC fluorescence were used. The sorted cells were used for a reverse transcription (RT)-PCR analysis.

RT-PCR

Total RNA was extracted from cells using an RNeasy Plus Micro Kit (QIAGEN), and cDNA was synthesized using a QuantiTect Whole Transcriptome Kit (QIAGEN) according to the manufacturer's instructions. PCR was performed using Ex Taq (Takara) and a thermal cycler (Veriti; Applied Biosystems). The thermocycle conditions were as follows: 10 s at 98°C, 15 s at the annealing temperature (*Robo1*, glyceraldehydes-3-phosphate dehydrogenase [GAPDH]: 62°C, *Robo2*: 63°C), and 30 s at 72°C for 25 cycles (*Robo1*, GAPDH) or 30 cycles (*Robo2*). The PCR products were separated on a 2% agarose gel and stained with ethidium bromide.

A quantitative real-time PCR analysis was performed using the SYBR green-labeling system (SYBR Premix Ex Taq II; Takara) and the ABI Prism 7700 Sequence Detection System (Applied Biosystems). Amplifications were performed in a 96-well optical plate, and the thermocycle conditions were as follows: 5 s at 95°C, 10 s at 62°C, and 30 s at 72°C for 40 cycles. The primers used were as follows: Robo1-F, 5′-CTCCCGTCTGATGACACACAATACC-3′; Robo1-R, 5′-CATTAAGGG TTAGG-CAATCAATCAGCAACAC-3′; Robo2-F, 5′-GCCCAGCTGCGG ATCACCTC-3′; Robo2-R, 5′-CCGGCCCCACCCCTTTTTCC-3′; GAPDH-F, 5′-GTCATCATCTCC-GCCCCTTCTGC-3′; GAPDH-R, 5′-GATGCCTGC TTCACCACCTTCTTG-3′. A quantitative analysis was performed using the delta–delta Ct method with GAPDH as an internal control.

Statistical Analysis

The data were evaluated using the Student *t*-test and the software package JSTAT. All values were expressed as the mean ± standard error of the mean, and *P*-values <0.05 were considered significant.

Results

Spatiotemporal Expression Patterns of Robo1 mRNA and Protein in the Developing Neocortex

To investigate the roles of *Robo1* in the developing neocortex, we first examined its expression in embryonic and postnatal mouse cortices by in situ hybridization (Fig. 1*A–F*). A signal for *Robo1* was detected in the preplate (PP) as early as E12.5 and, by E16.5, *Robo1* mRNA exhibited a layer-specific expression pattern within the CP. In situ hybridization using an *ER81* probe (a marker for layer V neurons) in adjacent sections indicated that *Robo1* mRNA is highly expressed in layer V neurons and moderately expressed in neurons of layers II/III and VI at P1 (Fig. 1*D* and data not shown). While the level of *Robo1* mRNA expression was maintained in deep-layer neurons (layers V and VI), its expression in the upper part of layers II/III was upregulated by P1, and remained high at P3 (Fig. 1*D,E*). Its expression gradually decreased after P7, but it was still detectable at P15 (Fig. 1*F* and data now shown).

The layer-specific expression pattern of *Robo1* mRNA in the CP suggested that these cells were pyramidal neurons. To assess the identity of the Robo1 expressing cells, we next examined the stage-dependent localization of Robo1 protein within pyramidal neurons. At E15.5, Robo1 protein was strongly expressed in the intermediate zone (IMZ) and weaker in the CP (Fig. 1*G–K*). At this stage, the cortical IMZ consists of corticofugal and thalamocortical axons, as well as tangentially migrating interneurons (Andrews et al. 2006, 2008; López-Bendito et al. 2007) and radially migrating pyramidal cells, making it difficult to discern the source of Robo1 protein expression. We, therefore, co-labeled Robo1 protein with a cortical callosal projection neuron marker, Satb2 (Alcamo et al. 2008; Britanova et al. 2008). We found that Robo1 protein was at times localized at the leading process of Satb2-expressing neurons in the IMZ and CP (Fig. 1*K,K′*), suggesting that it was expressed in migrating pyramidal neurons. We further examined the localization and distribution of Robo1 protein at E18.5 and P1 (Fig. 1*L–U′*). We found that, although *Robo1* mRNA was expressed in cells of layers V, VI, and upper part of layers II/III at these stages (Fig. 1*C,D*). Robo1 protein was predominantly detected in the MZ, and in a graded manner, in the cell somata of neurons within the CP (Fig. 1*N,S*). These data suggest that Robo1 protein mainly localizes in the neurites and axons after translation. We further assessed the co-localization of Robo1 protein with Satb2 whose expression is maintained in callosal projection neurons in the CP (Alcamo et al. 2008; Britanova et al. 2008). We found numerous examples of such co-localization (Fig. 1*P′,U′*). These results indicate that Robo1 is indeed expressed in differentiated pyramidal cells within the neocortex.

Suppression of Robo1 Expression in the Developing Mouse Neocortex

Our analyses revealed that Robo1 protein was expressed in a graded manner within the CP during critical stages of pyramidal cell migration and positioning (Fig. 1*K′,N,S*), and we wished to explore the requirement of this molecule in these events. We, therefore, analyzed *Robo1*$^{-/-}$ knockout mice to assess the effect of loss of *Robo1* in the distribution of neocortical neurons. We utilized a *Robo1* knockout line in which the whole *Robo1* gene (exons 1–22) is deleted (Andrews et al. 2008), and examined the cytoarchitecture of the adult neocortex by Nissl staining (Fig. 2*A*). Notably, in contrast to the organized alignment of neurons in the supragranular layers (layers II/III) of the *Robo1* wildtype cortex (Fig. 2*A*), *Robo1*$^{-/-}$ cortices exhibited dense cell distribution in layers II/III (Fig. 2*A*). We further quantified the density of cells in these

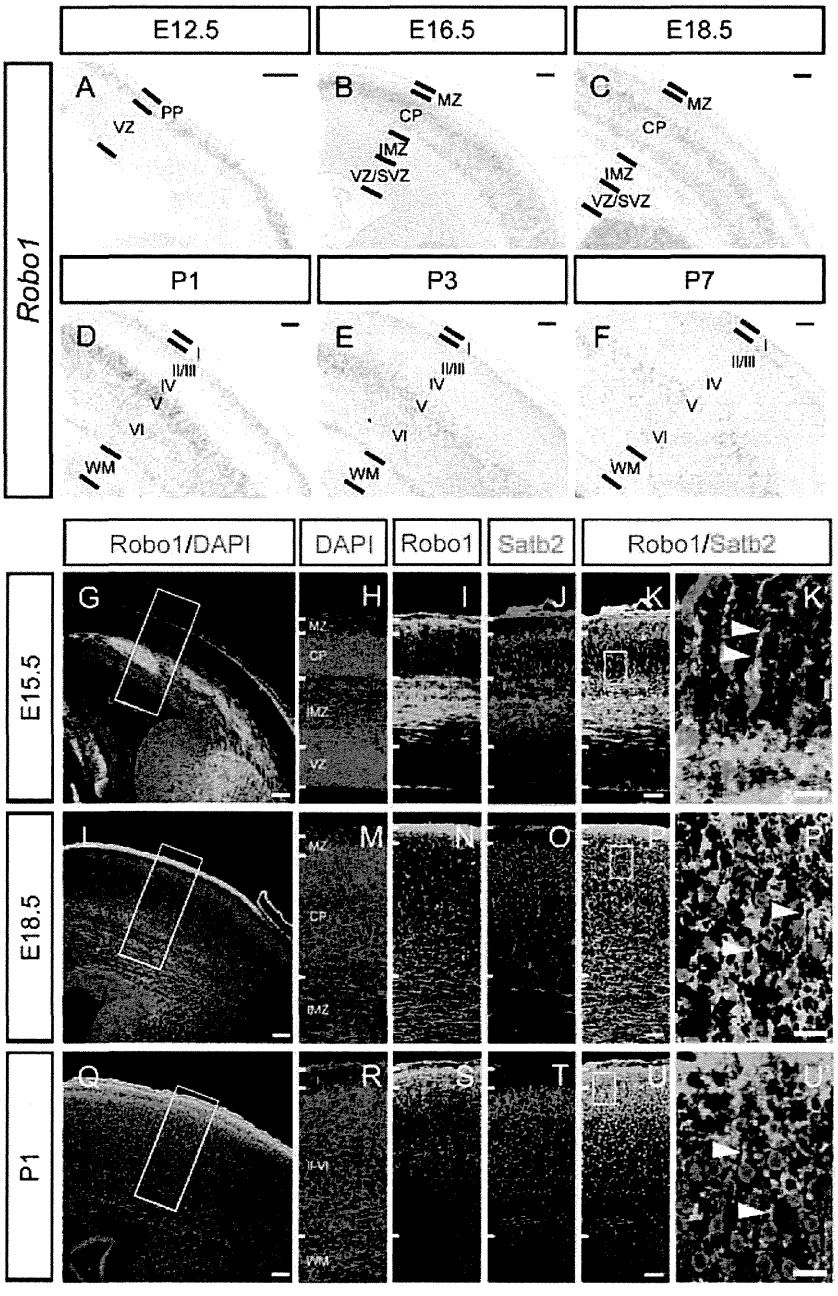

Figure 1. Temporal expression patterns of Robo1 in the developing mouse neocortex. (*A–F*) In situ hybridization of *Robo1* mRNA at embryonic (E12.5, 16.5, 18.5) and postnatal (P1, 3, 7) stages. (*G–U*) Immunohistochemistry of Robo1 in the developing mouse neocortex. Robo1, Satb2, and DAPI staining of coronal sections of the E15.5 (*G–K'*), E18.5 (*L–P'*), and P1 (*Q–U'*) neocortex. Middle panels (*H–K, M–P, R–U*) show higher magnification views of the boxed area in the left panels (*G, L, Q*), respectively. (*K', P', U'*) Higher magnification views of the boxed areas in (*K, P, U*), respectively. Arrowheads indicate neuronal processes with Robo1 expression. PP, preplate; MZ, marginal zone; CP, cortical plate; IMZ, intermediate zone; SVZ, subventricular zone; VZ, ventricular zone; I–VI, cortical layers I–VI; WM, white matter. Scale bars: (*A–F, G, L, Q*), 100 μm; (*H–J, M–P, R–U*), 50 μm; (*K', P', U'*), 10 μm.

layers in *Robo1*$^{-/-}$ cortices by counting the number of DAPI+ nuclei. Cell density was significantly higher in *Robo1*$^{-/-}$ cortical layers II/III than those in the *Robo1*$^{+/+}$ cortex (*Robo1*$^{+/+}$: 162.0 ± 5.9; *Robo1*$^{-/-}$: $214.1 \pm 11.2 \times 10^3$ cells/mm^3, $P < 0.01$, Fig. 2*B*). As we previously reported an increase in the total number of interneurons in the adult *Robo1*$^{-/-}$ cortex (Andrews et al. 2008), we next examined whether this increase in cell density in *Robo1*$^{-/-}$ cortical layers II/III attributes to any changes in pyramidal cell distribution, by utilizing a specific marker for layers II/III pyramidal cells, Cux1 (Fig. 2*D,E*, Nieto et al. 2004). Notably, the distributions of Cux1-expressing neurons in *Robo1*$^{-/-}$ cortices were significantly dense throughout layers II/III compared with that of control cortices (bins 2–5, $n = 12$ sections, $P < 0.05$, Fig. 2*E*). To determine whether this change is due to altered distribution or increased proliferation, we quantified the total number of Cux1-expressing cells within layers II/III in *Robo1*$^{-/-}$ cortices. We observed no changes in the total Cux1-positive cell number in *Robo1*$^{-/-}$ cortices (Fig. 2*F*), indicating that the observed increase in cell density in *Robo1*$^{-/-}$

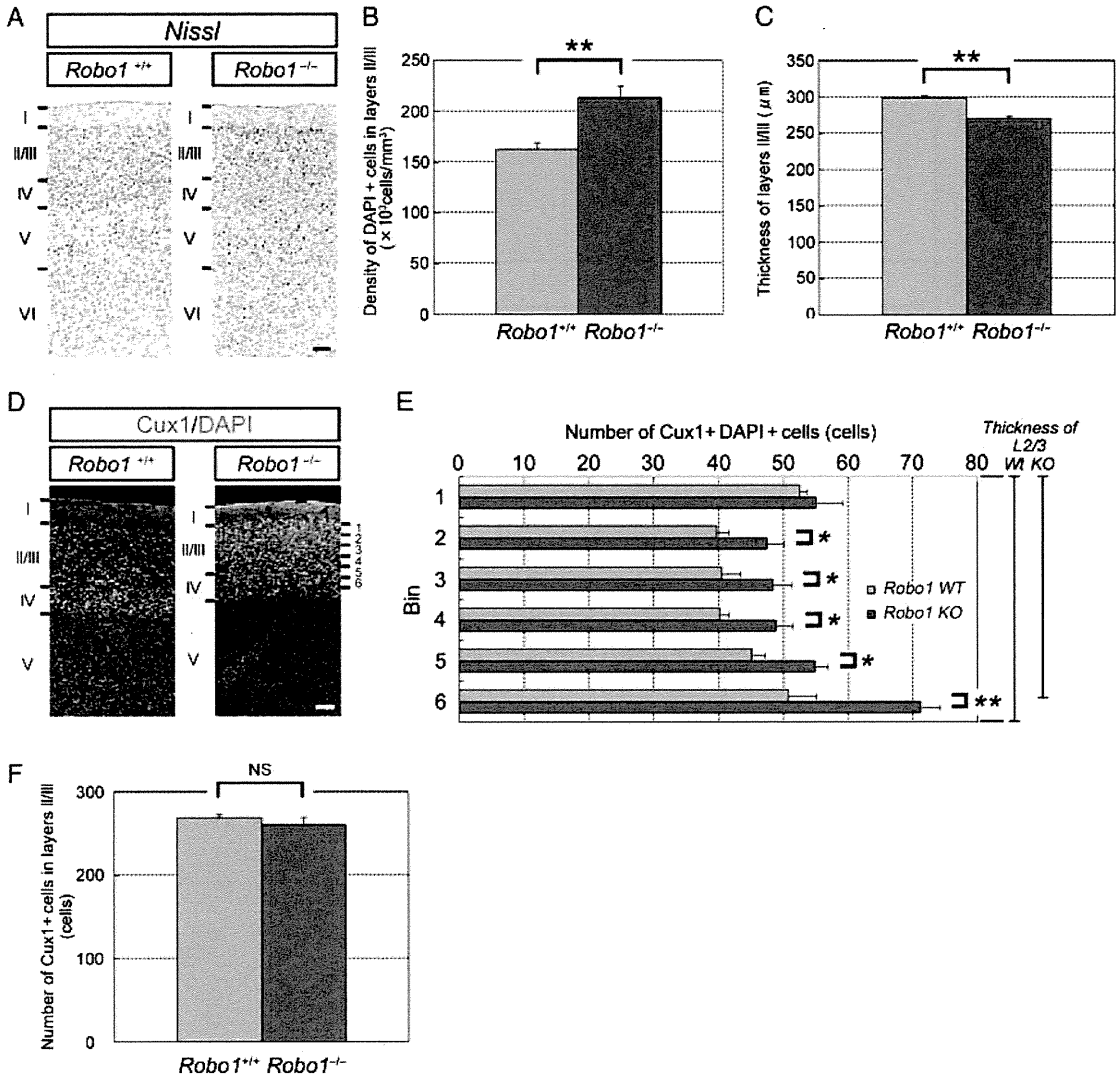

Figure 2. Laminar organization of the *Robo1*$^{-/-}$ knockout mouse neocortex. (*A*) Nissl staining images of the adult (P60) *Robo1*$^{+/+}$ and *Robo1*$^{-/-}$ neocortex. (*B* and *C*) Histograms of the average density of DAPI+ cells (*B*) and average thickness (*C*) of layers II/III in *Robo1*$^{+/+}$ and *Robo1*$^{-/-}$ littermate cortices. (*D*) Cux1 (green) immunohistochemistry and DAPI (blue) staining of the P58 *Robo1*$^{+/+}$ and *Robo1*$^{-/-}$ neocortex. (*E*) Quantitative analysis of the radial distribution of Cux1/DAPI double-positive cells in *Robo1*$^{+/+}$ and *Robo1*$^{-/-}$ cortices. For this quantification, layers II/III were divided into 6 equal bins according to their mean position in the *Robo1*$^{+/+}$ neocortex. The same bin was applied to the *Robo1*$^{-/-}$ cortex; however, due to the decrease in the thickness of layers II/III in the *Robo1*$^{-/-}$ cortex (C), bin 6 includes Cux1/DAPI double-positive cells of layer IV in the *Robo1*$^{-/-}$ cortex. (*F*) A histogram indicating the total number of Cux1-positive cells in layers II/III of *Robo1*$^{-/-}$ and *Robo1*$^{+/+}$ littermate cortices. Scale bars: (*A* and *D*), 100 μm. WT, wildtype; KO, knockout; NS, not significant. *$P < 0.05$, **$P < 0.01$.

attributes to changes in layers II/III pyramidal cell distribution, rather than increased proliferation and/or survival of these cells upon loss of *Robo1*. Consequently, the average thickness of layers II/III in the *Robo1*$^{-/-}$ cortex was significantly thinner as compared with *Robo1* wildtype controls (*Robo1*$^{+/+}$: 299.1 ± 3.9; *Robo1*$^{-/-}$: 270.2 ± 4.1 μm, $P < 0.05$, Fig. 2*C*), resulting in a superficial shift of layer IV toward the pial surface (Fig. 2*D*,*E*; note that bin 6 in Fig. 2*E* includes Cux1-positive layer IV cells in the *Robo1*$^{-/-}$ cortex but not the *Robo1*$^{+/+}$ cortex). Together, these observations further supported the idea that Robo1 is required for normal laminar formation by upper-layer neurons, in particular layers II/III pyramidal cells.

Thus, to clarify the cell-autonomous requirement of Robo1 in the laminar distribution of layers II/III neurons, we directly suppressed its expression in a discrete population of cortical pyramidal cells using RNA interference. We designed 4 *Robo1*-shRNA-expression vectors (*Robo1*-shRNA1–4) to target distinct regions in the Robo1 coding sequence (Supplementary Fig. S1*A*). These vectors were co-transfected with *Robo1*-expression vector into COS7 cells and the expression of recombinant Robo1 protein were examined. *Robo1*-shRNA1 and *Robo1*-shRNA4 greatly reduced the amount of Robo1 protein expression (Supplementary Fig. S1*B*), whereas *Robo1*-shRNA2 and *Robo1*-shRNA3 had weaker effects (data not shown). The introduction of a mutation within the Robo1 target region in *Robo1*-shRNA1 (Mt-*Robo1*-shRNA1) abolished the knockdown effect of *Robo1*-shRNA1 (Supplementary Fig. S1*C*). We further confirmed that *Robo1*-shRNA1 had a little effect on Robo2 expression (Supplementary Fig. S1*D*); consequently, *Robo1*-shRNA1 was used in subsequent experiments.

To confirm the effect of *Robo1*-shRNA1 in vivo, we introduced *Robo1*-shRNA1 together with EGFP-expression vector

(pCAGGS-EGFP) into the lateral ventricle of E15.5 embryos using in utero electroporation. At P1, reduced Robo1 protein expression was observed in EGFP-positive cells transfected with *Robo1*-shRNA compared with control-shRNA in the mouse cortex (Supplementary Fig. S1*E*). We further isolated EGFP-positive cells from the P1 mouse neocortex using FACS, and examined *Robo1* mRNA expression by quantitative RT-PCR analysis (Supplementary Fig. S1*F*). *Robo1* mRNA expression level in the *Robo1*-shRNA-transfected cells was significantly reduced than that in the control cells (Supplementary Fig. S1*F*), whereas *Robo2* mRNA expression was unaffected (Supplementary Fig. S1*F*). We further examined the amount of total Robo1 protein by dissecting EGFP-expressing neocortical tissues at P1. The amount of Robo1 protein was also significantly decreased by immunoblot (Supplementary Fig. S1*G*). Together, these results indicate that *Robo1*-shRNA1 does effectively reduce the expression of endogenous Robo1 in vivo.

Robo1-Suppressed Neurons Exhibit a Delay in their Migration to the Cortical Plate

To investigate the role of Robo1 in the development of neocortical layers II/III pyramidal neurons, we introduced *Robo1*-shRNA1 or control-shRNA together with pCAGGS-EGFP into the lateral ventricle of E15.5 embryos using in utero electroporation as described above. Previous studies demonstrated that newborn neurons generated in the VZ at E15.5 differentiate into projection neurons of layers II/III (Hatanaka et al. 2004). To validate the specificity of shRNA transfection in cortical pyramidal cells, we examined the expression of cell type markers, Satb2 (cortical callosal projection neuron marker; Alcamo et al. 2008; Britanova et al. 2008), calbindin (cortical interneuron marker; Anderson et al. 1997), and GFAP (astrocyte marker; DeArmond et al. 1980) in EGFP-positive cells by immunohistochemistry (Supplementary Fig. S2). We found the co-expression of EGFP with Satb2-positive (Supplementary Fig. S2*C*,*F*), but not calbindin-positive (Supplementary Fig. S2*I*,*L*), or GFAP-positive (Supplementary Fig. S2*O*,*R*) cells, demonstrating that *Robo1*-shRNA electroporation into the lateral ventricle at E15.5 specifically targets layers II/III pyramidal cells without affecting their neuronal identity.

Since the laminar organization was disrupted in the *Robo1*$^{-/-}$ cortex (Fig. 2), we selectively suppressed Robo1 in layers II/III neurons and examined their positions at the early postnatal period. Specifically, when *Robo1*-shRNA constructs were electroporated at E15.5 and examined at P1, >35% of EGFP-positive cells reached the superficial portion of the CP (bin 1) in control cortices (Fig. 3*A*,*B*). By contrast, in *Robo1*-shRNA1-transfected cortices, about 25% of EGFP-positive cells reached the superficial part of the CP (bin 1) at P1, but many cells were diffusely distributed throughout the CP (Fig. 3*A*,*B*). A similar result was obtained using *Robo1*-shRNA4 (Fig. 3*A*). These results suggest that suppression of *Robo1* may cause a delay in neuronal migration toward the pial surface.

To address this, we assessed the localization of EGFP-positive cells at earlier time point post-electroporation. We labeled neurons born at E15.5 by injecting EdU into pregnant dams 30 min prior to shRNA electroporation. The positions of both EdU single-labeled and EdU/EGFP co-labeled neurons were assessed at E18.5 (Fig. 4). Consistent with a previous report (Hatanaka et al. 2004), many E15.5 EGFP-transfected neurons that co-labeled with EdU have entered the CP in control cortices at E18.5 (Fig. 4*A*,*A*′, 50.7% in bins 1–8 in Fig. 4*C*). In contrast, we observed only few EdU+/EGFP+ cells entering the CP in *Robo1*-shRNA1-transfected cortices at this stage (Fig. 4*B*,*B*′, 25.5% in bins 1–8 in Fig. 4*C*), whereas EdU +/EGFP-cells were unaffected (Fig. 4*A*′,*B*′,*C*). Together, these data indicate that Robo1 suppression causes a delay in upper-layer pyramidal neuron migration, by affecting the timing of entry into the CP.

Robo1 is Required for Inside-Out Segregation of Layers II/III Pyramidal Cells

Our results demonstrate that loss of Robo1 affects the early phase of radial migration of layers II/III pyramidal neurons. To further explore the positioning defect caused by *Robo1* suppression at later stages, we assessed the distribution of *Robo1*-shRNA-transfected neurons at P4, P8, P12, and P15 (Fig. 5). At P4, most EGFP-positive cells of *Robo1*-shRNA-transfected cortices have finally reached the superficial portion of the CP; however, a small number of EGFP-positive cells were still present in middle, and deeper positions (Fig. 5*A* and data not shown). These results indicate that although *Robo1*-shRNA-transfected neurons exhibit a delay in entering the CP, these neurons are still capable of migrating to the outermost position of the CP, regardless of suppression of *Robo1*. However, after P8, many EGFP-positive cells were located in the upper portion of layers II/III beneath the MZ (Fig. 5*A*,*B*), showing a distribution substantially different from control neurons. Whereas control EGFP-positive neurons were distributed throughout the mid- to upper portion of layers II/III (bins 1–3 in Fig. 5*B*), *Robo1*-shRNA1 transfected were predominantly located in the most superficial part (bin 1) of these layers (P8; control: 40.0 ± 3.6% in bin 1 and 55.6 ± 1.7% in bin 2, *Robo1*-shRNA1: 83.3 ± 3.4% in bin 1 and 13.5 ± 1.6% in bin 2, $n = 12$ sections, $P < 0.01$, P15; control: 49.5 ± 5.8% in bin 1 and 41.4 ± 1.3% in bin 2, *Robo1*-shRNA1: 84.7 ± 2.7% in bin 1 and 13.6 ± 2.1% in bin 2, $n = 12$ sections, $P < 0.01$). Such differences were not observed in the Mt-*Robo1*-shRNA1-transfected cells (data not shown). To further assess whether the positional changes in *Robo1*-shRNA1-transfected cells were caused by specific suppression of *Robo1* expression, we transfected *Robo1* cDNA (pCAGGS-Robo1) together with *Robo1*-shRNA1 and pCAGGS-EGFP into the lateral ventricle of the E15.5 cortex. Radial distribution patterns of *Robo1*-shRNA1 plus *Robo1* cDNA-transfected EGFP-positive cells were identical to those of control-shRNA-transfected cells in this case (data not shown). These results indicate that the distinct localization observed in *Robo1*-shRNA1-transfected cells was caused by a specific suppression of *Robo1* expression.

Our results have so far demonstrated that within layers II/III pyramidal cells, suppression of *Robo1* expression causes: 1) delay in neurons to enter the CP; 2) relatively normal radial migration, where *Robo1*-suppressed neurons eventually reach the upper CP by P4; and 3) abnormal distribution of neurons after the first postnatal week, where neurons take up the outermost positions in the CP immediately underneath the MZ. Together, these results indicate that loss of Robo1 has a significant impact on the positioning of layers II/III neurons

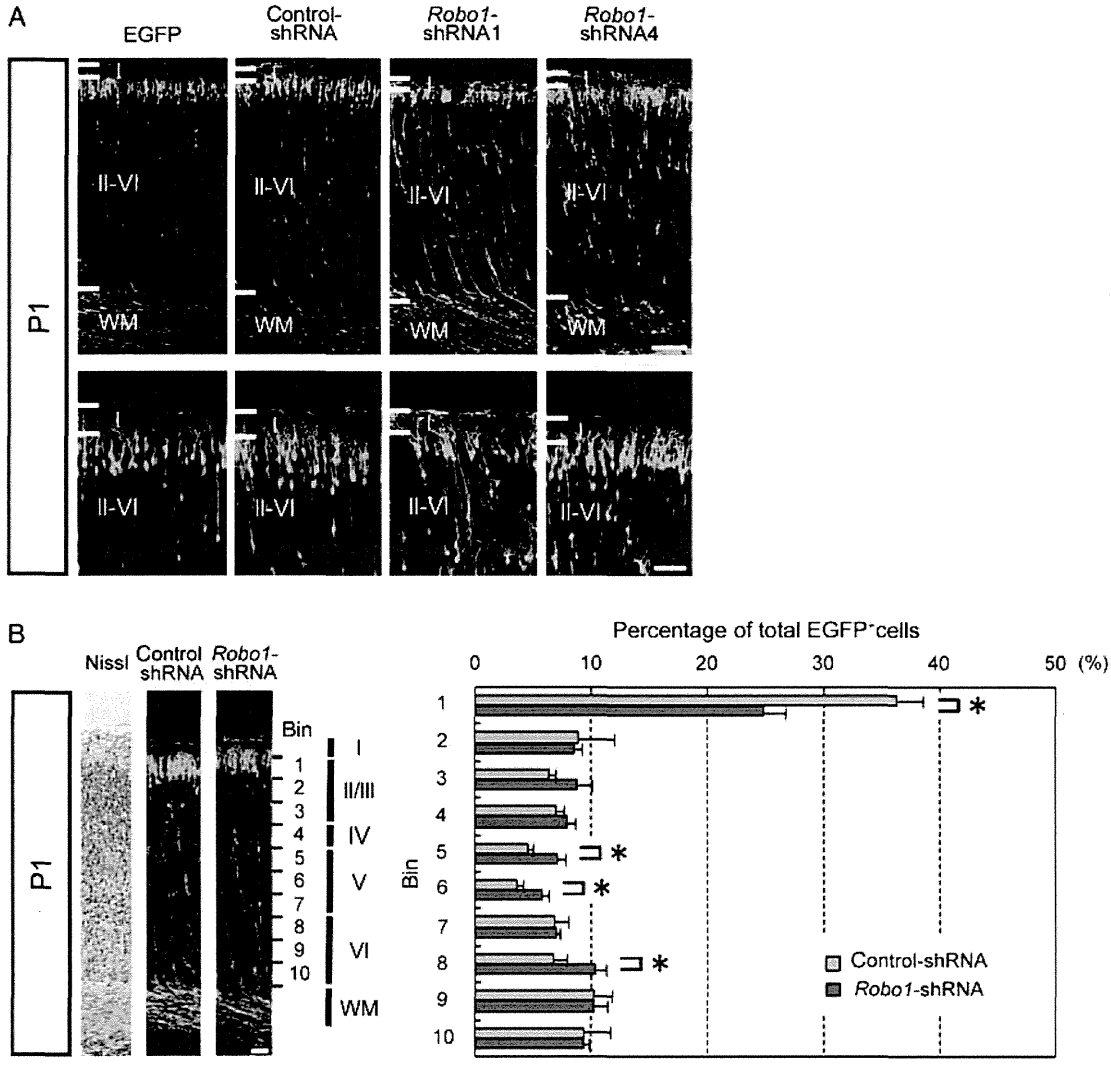

Figure 3. Localization of *Robo1*-suppressed cells in the P1 mouse neocortex. (*A*) Analysis of the distribution of control- and *Robo1*-shRNA-transfected EGFP-positive cells in the neocortex at P1. Bottom panels indicate the higher magnification images of upper neocortical regions in the top panels. (*B*) Quantitative analysis of the radial distribution pattern of control- and *Robo1*-shRNA-transfected EGFP-positive cells in P1 mice. Nissl-staining (left panel) and EGFP-staining (middle 2 panels) images are shown. (Right panel) Neocortical layers II/III and IV were divided into 10 equal bins and the number of EGFP-positive cells in each bin was counted. $^*P < 0.05$. Scale bars: top panels in (*A*), 100 μm; bottom panels in (*A* and *B*), 50 μm.

even after they have reached the pial surface. It is known that pyramidal neurons of the neocortex follow an inside-out neuronal distribution, where later-born neurons migrate past earlier-born cells to dominate a more superficial position within the CP. However, the cell and molecular mechanism by which the relative positioning of these neurons is established remains unclear (Magdaleno et al. 2002; Yoshida et al. 2006; Cooper 2008; Kubo et al. 2010). Since *Robo1*-suppressed cells appear to localize to the most superficial region within the neocortex, even after the first postnatal week (Fig. 5*A*,*B*), when the layer organization has been well-defined (Auladell et al. 1995), we next assessed the distribution pattern of temporal cohorts of neurons by performing sequential in utero electroporation analysis. When control-shRNA was transfected with pCAGGS-EGFP at E16.5, the majority of EGFP-positive neurons gave rise to the uppermost layers II/III neurons in the neocortex (bin 1 in Supplementary Fig. S3), whereas electroporation at E17.5 resulted in mainly gliogenesis (data not shown). This indicated that electroporation at E16.5 targets the latest cohorts of layers II/III pyramidal cells in the neocortex. We, therefore, co-electroporated control-shRNA or *Robo1*-shRNA1 together with pCAGGS-EGFP vector at E15.5, and the same cortices were subsequently electroporated with same shRNA constructs together with pCAGGS-DsRed at E16.5 (Fig. 6). As expected, control-shRNA-transfected cortices exhibited a typical inside-out distribution of temporal neuronal cohorts at P8, where E16.5 control-shRNA-electroporated DsRed-positive cells were localized superficial to E15.5 control-shRNA-electroporated EGFP-positive cells (Fig. 6*C*). Notably, *Robo1*-suppressed layers II/III neurons did not exhibit a characteristic inside-out distribution and, instead, later-born neurons were intermingled within the residual space that was unoccupied by E15.5-transfected EGFP-positive neurons (Fig. 6*F*). Furthermore, both E15.5 and E16.5 *Robo1*-shRNA-transfected neurons exhibited a dense distribution in the radial extent of the CP, resulting in a more compact lamina of electroporated cells, similar to that of

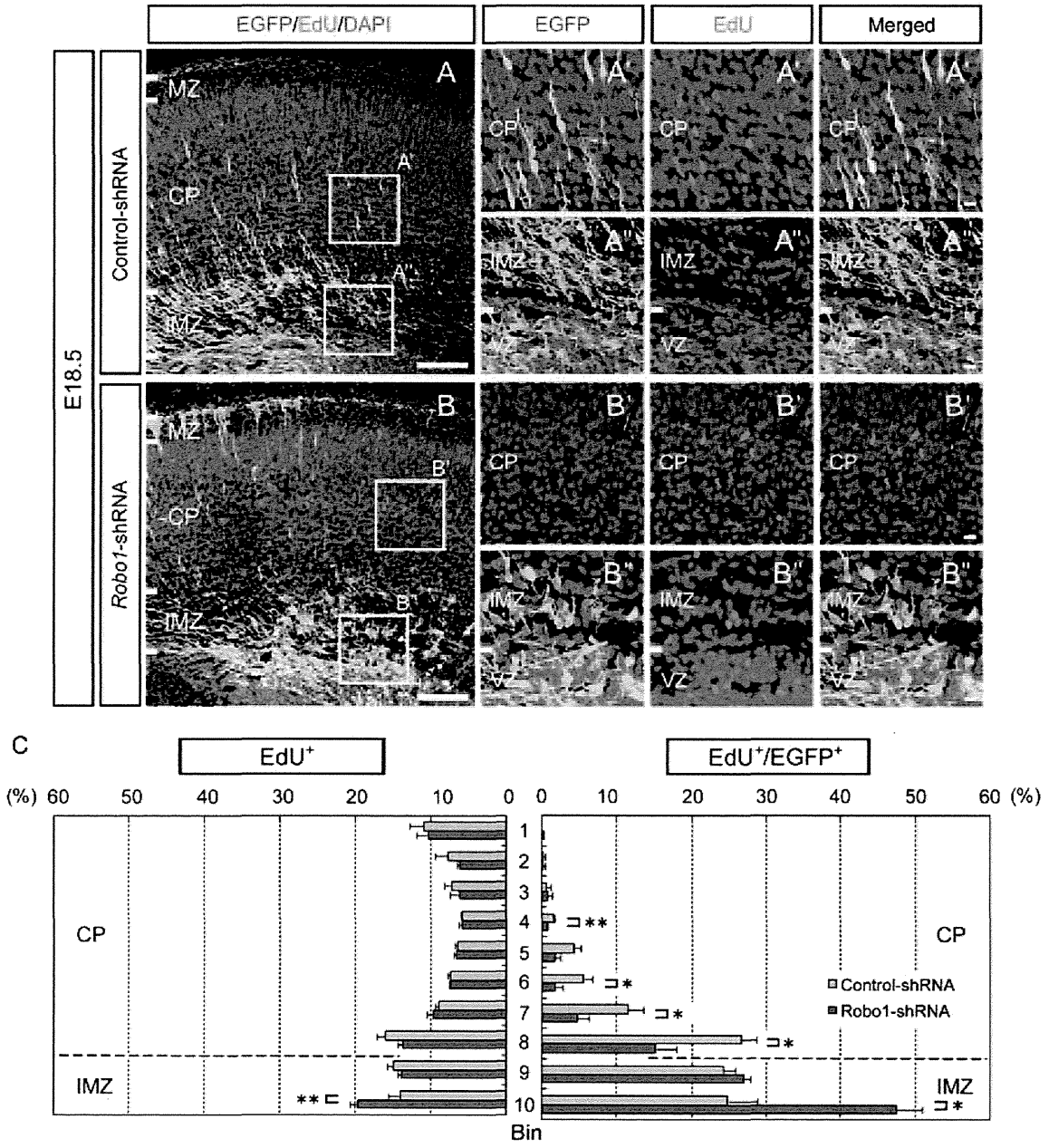

Figure 4. Localization of E15.5 born *Robo1*-suppressed neurons in the E18.5 neocortex. EGFP and EdU detection in the E18.5 neocortex transfected with (*A*) control-shRNA or (*B*) *Robo1*-shRNA1 at E15.5 with a pulse of EdU injection. (*A′*, *A″*) and (*B′*, *B″*) higher magnification views of boxed regions shown in (*A* and *B*). (*C*) Quantitative analysis of the radial distribution pattern of EdU-positive (left panel) or EdU/EGFP double-positive cells (right panel) in E18.5 mice. The cortical IMZ to MZ were divided into 10 equal bins and the number of EdU-positive or EdU/EGFP double-positive cells in each bin was counted. Dashed line indicates the border between the IMZ and CP. Scale bars: (*A* and *B*) 100 μm; (*A′*, *A″*, *B′*, *B″*) 10 μm. $^{*}P < 0.05$, $^{**}P < 0.01$.

upper CP neurons observed in the *Robo1* null cortex (Fig. 2). Together, these results indicate that upper-layer pyramidal neurons require Robo1 for their correct positioning and inside-out segregation within the CP.

We further examined whether suppression of Robo1 expression has any effect in the dendritic development of cortical pyramidal neurons, by assessing EGFP-positive cells located in layers II/III of E15.5 *Robo1*-shRNA-transfected cortices (Fig. 7). Although differences in morphology between *Robo1*-shRNA- and control-shRNA-transfected EGFP-positive cells were not apparent at P4 (Fig. 7*A*), marked differences in the growth and branching of neurites were observed at a subsequent stage. At P8, *Robo1*-shRNA1-transfected cells exhibited a more complex neurite branching at the apical side than control-shRNA-transfected cells (Fig. 7*A*). Quantitative analysis revealed that the number of neurites at the apical side in *Robo1*-suppressed cells was significantly larger than that in control cells (control: 1.4 ± 0.2, *Robo1*-shRNA1: 5.0 ± 0.4, $n = 25$ cells, $P < 0.01$), whereas no difference was observed at the basal side (control: 2.5 ± 0.2, *Robo1*-shRNA1: 2.7 ± 0.4, $n = 25$ cells, $P < 0.01$) (Fig. 7*B*). To further assess whether distinctive positioning and neuronal morphology of *Robo1*-suppressed cells were secondary effect to changes in their identity after migrating to their final position, we

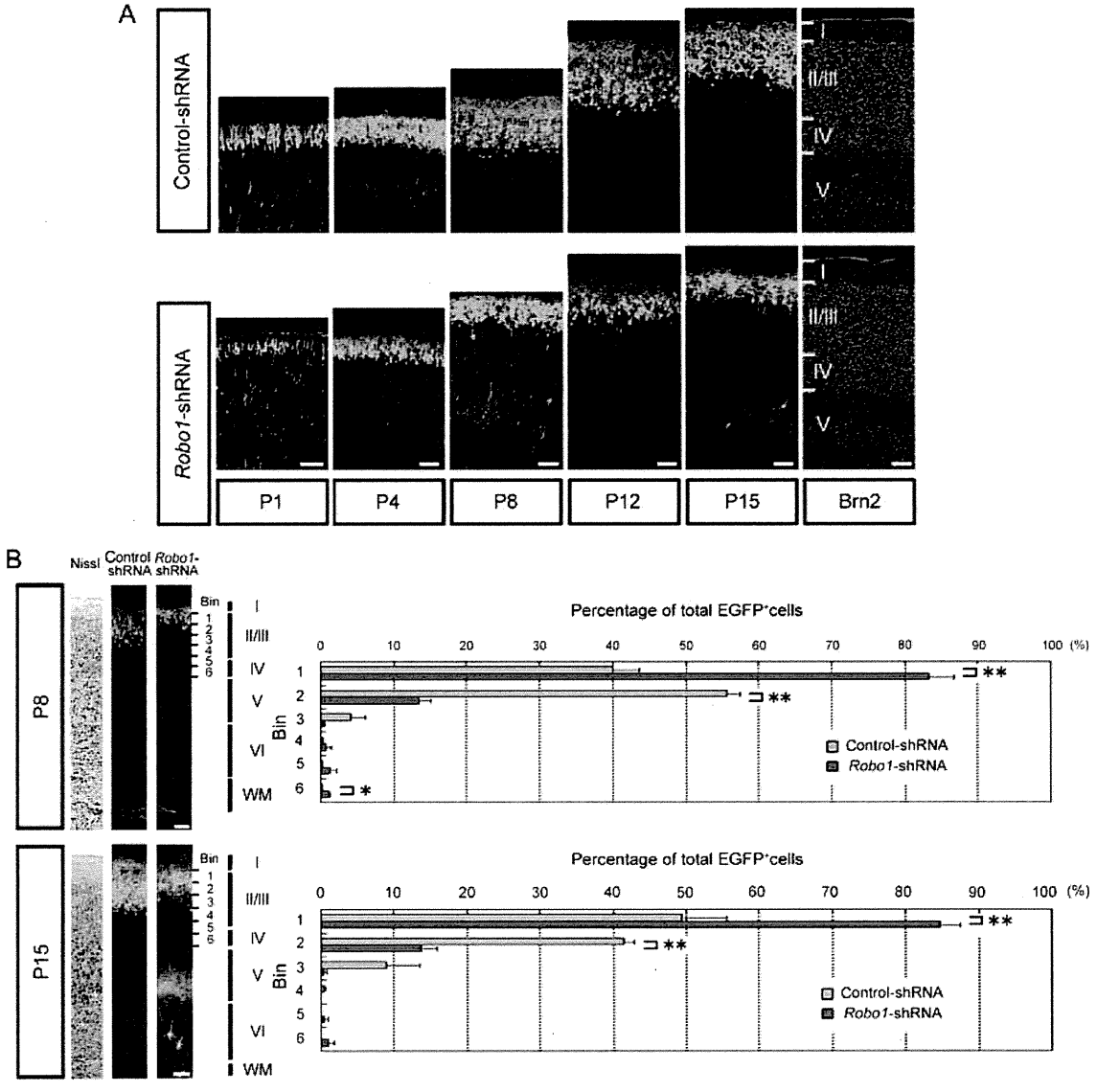

Figure 5. Localization of *Robo1*-suppressed cells in the developing neocortex. (*A*) Temporal analysis of the distribution of control- and *Robo1*-shRNA-transfected EGFP-positive cells in the neocortex. The right panels show Brn2 staining in the adjacent section of the P15 cortex indicating layers II–IV. (*B*) Quantitative analysis of the radial distribution pattern of EGFP-positive cells in P8 and P15 mice. Nissl-staining (left panels) and EGFP-staining (middle panels) images are shown. (Right panels) Neocortical layers II/III and IV were divided into 6 equal bins and the number of EGFP-positive cells in each bin was counted. $^{*}P < 0.05$, $^{**}P < 0.01$. Scale bars: 100 μm.

examined the expression of cell type specific markers in EGFP-positive cells at P8. Immunohistochemical analysis revealed that these cells express Brn2 (layers II/III pyramidal neuron marker) and NeuN (neuronal marker), but not GFAP, similar to control EGFP-positive cells (data not shown). Together with the analysis of short-term fate mapping of *Robo1*-shRNA1-transfected cells (Supplementary Fig. S2), these results demonstrate that *Robo1*-suppressed neurons show distinctive positioning without an overt change in their identity.

To further validate the specific requirement for Robo1 in the distribution of layers II/III pyramidal cells, we next manipulated Robo1-expression levels within cortical upper-layer neurons, and assessed their effect on neuronal positioning. Our earlier expression studies indicated that *Robo1* mRNA was normally expressed in layer V neurons at a higher level than those observed in layers II/III neurons (Fig. 1*D*). Therefore, one possibility is that the level of Robo1 expression may determine the final positions of pyramidal cells in a layer subtype-specific manner. To test this possibility, we electroporated pCAGGS-*Robo1* into the E15.5 embryo neocortex, and examined the positions of EGFP-positive cells at P8 (Supplementary Fig. S4). Upon introduction of pCAGGS-*Robo1*, we detected higher levels of Robo1 protein expression in the VZ, IMZ, and CP when compared with control cortices transfected with pCAGGS (Supplementary Fig. S4*A* and data not shown), whereas the position of EGFP-positive cell showed no significant changes in their distribution patterns (Supplementary Fig. S4*B*,*C*). These results showed that *Robo1*-overexpressing layers II/III neurons do not exhibit a shift to a deeper position as that of layer V neurons within the CP. Notably, however, we found an increase in the numbers of EGFP-positive axons projecting into the striatum (Supplementary Fig. S5*D*), which were normally

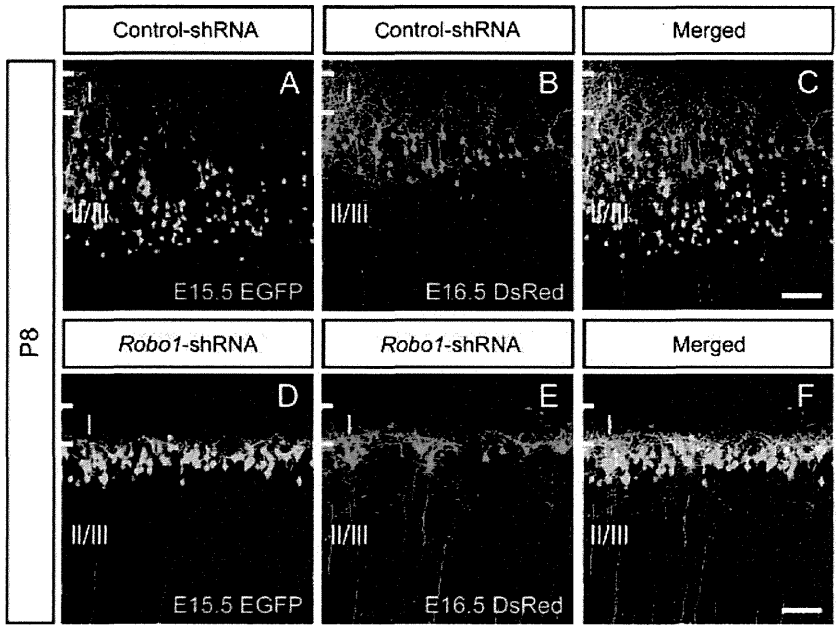

Figure 6. Distribution analysis of temporal cohorts of *Robo1*-suppressed neurons. Control-shRNA (*A–C*) or *Robo1*-shRNA1 (*D–F*) were electroporated together with pCAGGS-EGFP at E15.5 (*A* and *D*), and the same shRNA constructs were electroporated in the same cortex together with pCAG-DsRed at E16.5 (*B* and *E*). Distributions of neurons were examined at P8. Scale bars: 100 μm.

not observed in control EGFP-transfected layers II/III neurons (Supplementary Fig. S5*B*). These results implied that Robo1-expression levels may be important for refining the axonal projection patterns within distinct layer subtypes. Finally, we transfected *Robo1*-shRNA in mouse neocortices at E14.5, where the majority of neurons consists of layer IV neurons that do not normally express *Robo1* at perinatal stages (Fig. 1), and compared the positions of electroporated cells at P8. In these cases, the laminar distribution patterns and morphology of both *Robo1*- and control-shRNA-transfected cells were identical (Fig. 8*C,F*). These results indicate that layers II/III neurons have a specific requirement for Robo1 in their normal distribution, consistent with the restricted expression of Robo1 within the upper-layer neocortex.

Discussion

To date, growing numbers of genes have been identified that control the movement of neocortical neurons during the early steps of their radial migration (Caviness and Rakic 1978; Walsh and Goffinet 2000; Tsai and Gleeson 2005; Huang 2009; Honda et al. 2011). In contrast, the mechanisms by which neuronal distribution of neocortical pyramidal cells is controlled during terminal stages of migration have remained largely elusive. Here, using an in vivo loss-of-function approach with RNA interference and *Robo1* knockout mice, we directly demonstrate that *Robo1* expressed in upper-layer pyramidal neurons plays a significant role in determining their positions within the neocortex.

Robo1 Regulates the Laminar Distribution of Layers II/III Pyramidal Cells

Our studies show that Robo1 is expressed in layers II/III pyramidal neurons during the critical period of their migration and final positioning. Notably, while the level of *Robo1* mRNA expression remains constant in deep-layer neurons (layer V), its expression in the upper part of layers II/III is upregulated during the early postnatal period (Fig. 1). Moreover, Robo1 protein is predominantly distributed in the apical neurites of these neurons and primarily near the MZ (Fig. 1*P′*, *U′*). In agreement with its expression pattern, we found that Robo1 plays a critical role in the positioning of these neurons during postnatal stages, where the major changes in the neuronal distribution of *Robo1*-suppressed layers II/III pyramidal cells occur between P4 and P8 (Fig. 5*A*). This implies that possible interactions between Robo1 and other molecules during the first postnatal week may be crucial in determining the final positions of these cells, with those that lack Robo1 failing to descend to deeper positions in the CP.

What, then, is the cellular mechanism by which Robo1 regulates the correct positioning of layers II/III pyramidal neurons? In principle, the precise inside-out distribution of temporal cohorts of cortical neurons can be achieved through a number of different mechanisms. Most simply, Robo1 may regulate correct positioning of layers II/III neurons by promoting their early migration (Fig. 4), as delay in entering the CP would result in their more superficial positioning. However, although our results demonstrate that loss of Robo1 affects the time of entry of layers II/III neurons into the CP, hence early migration is delayed, we found that most E15.5 *Robo1*-suppressed cells are able to reach the pia by P4, when positional defects are least prominent. Furthermore, if all *Robo1*-suppressed cells were delayed in their migration in a similar manner, one would expect such cells born at E15.5 to take deeper positions within the CP than cells born at E16.5. However, this appears not to be the case in the sequential electroporation experiments (Fig. 6). As such, these results imply that neuronal positioning of layers II/III pyramidal neurons requires later action of Robo1 after they reach the

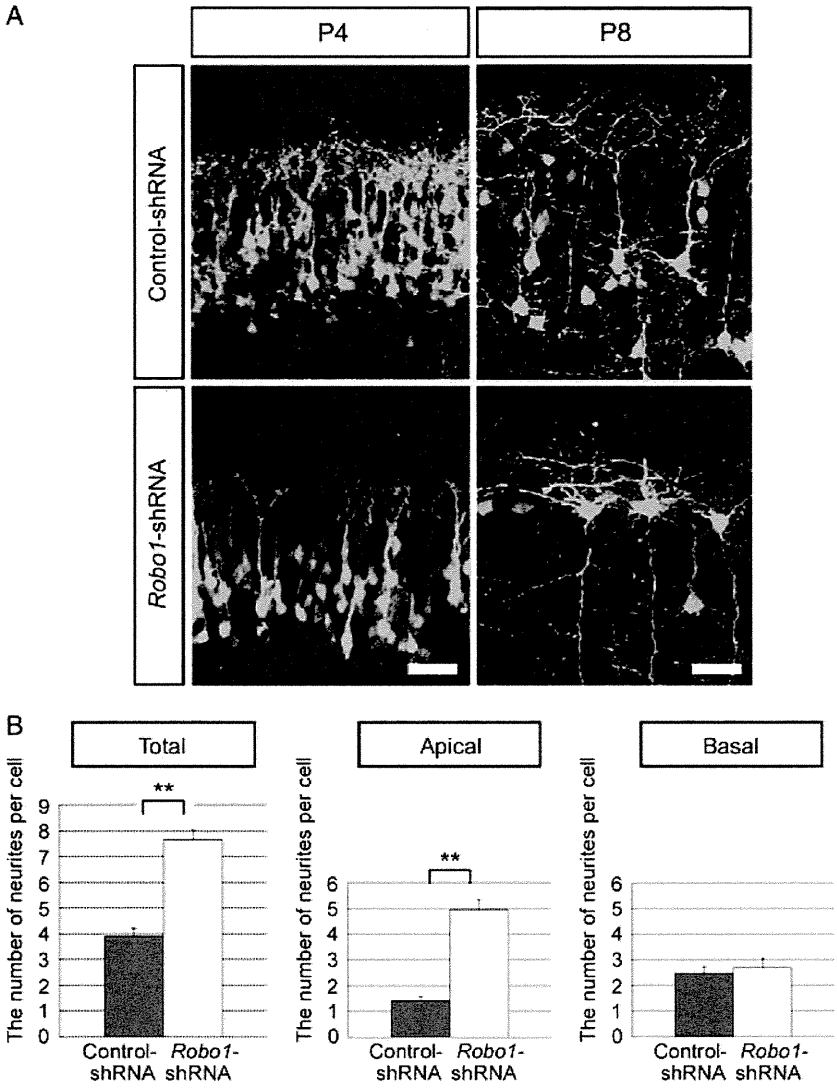

Figure 7. Morphological analysis of *Robo1*-shRNA-transfected cells in the developing neocortex. (*A*) Representative images of control- and *Robo1*-shRNA-transfected EGFP-positive cells in the neocortical sections of P4 and P8 mice. (*B*) Quantitative analysis of the number of neurites per cell transfected with control- and *Robo1*-shRNA. $^{**}P < 0.01$. Scale bars: 50 μm.

pial surface, rather than simply carrying over the migration delay from earlier development.

It has been proposed that the interaction between migrating neurons and the molecules expressed in the MZ has a prominent influence in facilitating or ceasing neuronal migration at the appropriate time. By far the most studied, extracellular matrix glycoprotein Reelin and its signaling pathway play critical roles in radial migration and influences the outcome of neocortical layer formation (Caviness and Sidman 1973; D'Arcangelo et al. 1995; Ogawa et al. 1995; Howell et al. 1997; Sheldon et al. 1997). Notably, the phenotype caused by *Robo1* suppression is clearly distinct from that of known Reelin pathway interference analysis (Trommsdorff et al. 1999; Olson et al. 2006; Feng et al. 2007; Hack et al. 2007; Hashimoto-Torii et al. 2008; Yano et al. 2010; Franco et al. 2011; Sekine et al. 2011). Whereas *reelin* and *Dab1* mutant mice exhibit an inverted laminar neuron distribution, cells of layers II/III that lack Robo1 expression appear to be anchored to the most superficial part of the CP, beneath the MZ. One possibility is that the detachment of migrating pyramidal neurons from radial glial fibers may be affected in the absence of Robo1 through misregulation of cell–cell and cell–substrate adhesion molecules. Although we did not observe obvious clusters of radial glia-associated *Robo1*-suppressed cells in our analysis, it has been demonstrated that Slit/Robo signaling inhibits cell adhesion during neurite outgrowth and axon extension in chick neural retina (Rhee et al. 2002, 2007). Thus, Robo signaling may also play a role in the adhesive interaction between cortical pyramidal cells and radial glia through similar mechanisms.

A second and intriguing hypothesis is that Robo1 may regulate correct positioning of layers II/III neurons through their dendritic development. Following detachment from radial glia, pyramidal cells extend apical dendrites and elaborate branching toward their target layers depending on the position of their cell body (Barnes and Polleux 2009). In our studies, *Robo1*-suppressed layers II/III pyramidal cells exhibited dense distribution in the radial extent of CP when compared with that of control cells (Figs 2 and 6). These observations suggest that the failure of *Robo1*-suppressed

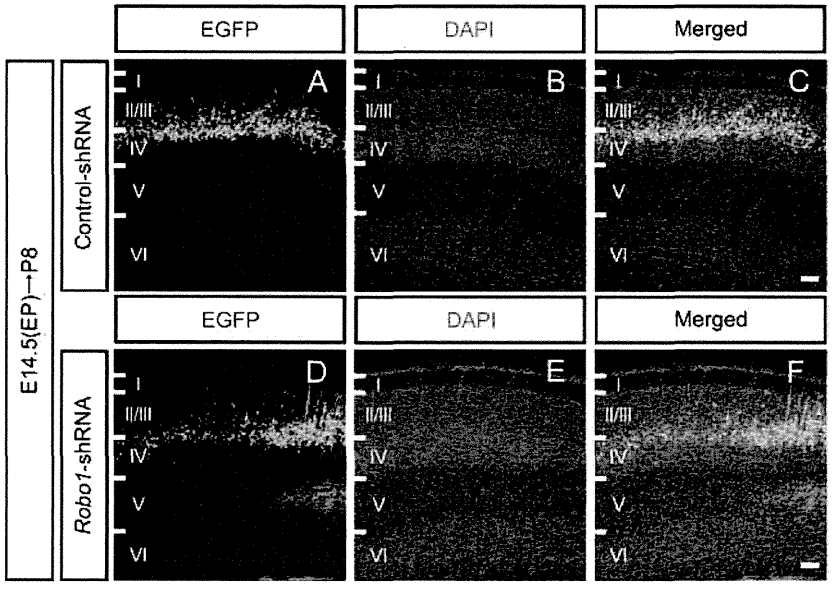

Figure 8. Distribution of EGFP-positive cells of the P8 mouse neocortex transfected with control-shRNA (*A–C*) or *Robo1*-shRNA1 (*D–F*) at E14.5. EP, electroporation. Scale bars: 100 μm.

neurons to interact with local cues may prohibit their normal dendritic extension, which leads to abnormally dense neuronal distribution along the radial axis (Fig. 6*F*). In *Robo1*-suppressed layers II/III cells, their superficial positioning may not be the primary cause of the changes in their dendritic morphology, as both E16.5 control- and *Robo1*-shRNA-transfected cells showed similar neuronal distributions (Supplementary Fig. S3), but the morphological differences were still apparent (Fig. 6*E*). Indeed, it has been suggested that defect in dendritogenesis may be instructive, rather than a result of perturbed layer formation (Teng et al. 2001; Olson et al. 2006; Nichols and Olson 2010; Franco et al. 2011). Thus, further investigations on how distinctive dendritic patterning is achieved in *Robo1*-suppressed neurons (Fig. 7), may provide novel insights into understanding the relationship between dendritogenesis and fine-tuning of layer construction in the neocortex.

Requirement for Robo1 in Cortical Neuron Subtypes

Earlier studies on the role of *Robo1* in neocortical development have provided compelling evidence for its involvement in interneuron development and axonal path formation (Andrews et al. 2006, 2008; López-Bendito et al. 2007; Hernandez-Miranda et al. 2011). In contrast, the specific roles for Robo1 in upper-layer pyramidal neurons have remained elusive. Our RNA interference approach has enabled us to dissociate the requirement for Robo1 in the development of layers II/III pyramidal neurons, as they terminate migration and assume their final positions during the first postnatal week. Interestingly, although it has been suggested that later-born neurons may utilize a common migration strategy (Nadarajah et al. 2001; Hatanaka et al. 2004), our temporal electroporation analysis has revealed that E14.5 *Robo1*-shRNA-transfected cells, unlike that of E15.5 or E16.5 neurons, do not exhibit changes in their positioning (Fig. 8*F*). Our observation is consistent with a previous study that cortical neurons born at E14 have a distinct character from that of layers II/III neurons (Ajioka and Nakajima 2005). Since the majority of E14 born neurons adopt a layer IV fate (Takahashi et al. 1999) and do not express detectable levels of Robo1 (Fig. 1), these results imply that Robo signaling may act in a temporally and spatially restricted manner, where layer IV neurons are refractory to loss of Robo1 expression. Indeed, a new study examining the role of *Robo4*, a different Robo family receptor expressed in the neocortex reported that the laminar organization of the neocortex develop normally in cortex-specific *Robo4* knockout mice, but the radial migration of E14.5 *Robo4*-suppressed mouse cortical neurons was delayed (Zheng et al. 2011). These results highlight the importance of distinct Robo receptors in regulating neuronal migration and positioning in a layer-specific manner.

In summary, we have presented evidence that Robo1 regulates the positioning of layers II/III pyramidal neurons in the developing neocortex. Collectively with previous reports (Hatanaka et al. 2004; Hack et al. 2007), our current study suggests that although laminar identities of neurons may be largely determined at birth (McConnell and Kaznowski 1991), the mechanisms by which layer-specific neurons navigate to their final positions may involve cell type- and context-dependent combinatorial codes that further refine the formation of neocortical laminae.

Supplementary Material

Supplementary material can be found at: http://www.cercor.oxfourdjournals.org/.

Funding

This work was supported by grants from the Ministry of Health, Labor and Welfare of Japan and the Ministry of Education, Culture, Sports, and Science and Technology of Japan, Grant-in-Aid for Scientific Research on Innovative Areas "Neural Diversity and Neocortical Organization," from the Wellcome Trust (Program Grant 089775 to J.G.P. and W.D.A.) and from the Strategic Research Program for Brain Sciences "Understanding of molecular and environmental bases for brain health."

Notes

We thank Dr Fujio Murakami for generous gift of anti-Robo1 antibody, Dr Satoru Masuda for FACS experiment, Dr Shigeki Yuasa, and Dr Toshio Terashima for valuable advice and all members of the Hanashima Laboratory for valuable discussions. *Conflict of interest:* none declared.

References

Ajioka I, Nakajima K. 2005. Birth-date-dependent segregation of the mouse cerebral cortical neurons in reaggregation cultures. Eur J Neurosci. 22:331–342.

Alcamo EA, Chirivella L, Dautzenberg M, Dobreva G, Fariñas I, Grosschedl R, McConnell SK. 2008. Satb2 regulates callosal projection neuron identity in the developing cerebral cortex. Neuron. 57:364–377.

Anderson SA, Eisenstat DD, Shi L, Rubenstein JL. 1997. Interneuron migration from basal forebrain to neocortex: dependence on Dlx genes. Science. 278:474–476.

Andrews W, Barber M, Hernadez-Miranda LR, Xian J, Rakic S, Sundaresan V, Rabbitts TH, Pannell R, Rabbitts P, Thompson H *et al.* 2008. The role of Slit-Robo signaling in the generation, migration and morphological differentiation of cortical interneurons. Dev Biol. 313:648–658.

Andrews W, Lipai A, Plachez C, Camurri L, Zhang J, Mori S, Murakami F, Parnavelas JG, Sundaresan V, Richards LJ. 2006. Robo1 regulates the development of major axon tracts and interneuron migration in the forebrain. Development. 133:2243–2252.

Angevine JB, Jr, Sidman RL. 1961. Autoradiographic study of cell migration during histogenesis of cerebral cortex in the mouse. Nature. 192:766–768.

Auladell C, Martinez A, Alcantara S, Super H, Soriano E. 1995. Migrating neurons in the developing cerebral cortex of the mouse send callosal axons. Neuroscience. 64:1091–1103.

Barnes AP, Polleux F. 2009. Establishment of axon-dendrite polarity in developing neurons. Annu Rev Neurosci. 32:347–381.

Borrell V, Kaspar BK, Gage FH, Callaway EM. 2006. In vivo evidence for radial migration of neurons by long-distance somal translocation in the developing ferret visual cortex. Cereb Cortex. 16:1571–1583.

Britanova O, de Juan Romero C, Cheung A, Kwan KY, Schwark M, Gyorgy A, Vogel T, Akopov S, Mitkovski M, Agoston D *et al.* 2008. Satb2 is a postmitotic determinant for upper-layer neuron specification in the neocortex. Neuron. 57:378–392.

Caviness VS, Jr, Rakic P. 1978. Mechanisms of cortical development: a view from mutations in mice. Annu Rev Neurosci. 1:297–326.

Caviness VS, Jr, Sidman RL. 1973. Time of origin or corresponding cell classes in the cerebral cortex of normal and reeler mutant mice: an autoradiographic analysis. J Comp Neurol. 148:141–151.

Chen Z, Gore BB, Long H, Ma L, Tessier-Lavigne M. 2008. Alternative splicing of the Robo3 axon guidance receptor governs the midline switch from attraction to repulsion. Neuron. 58:325–332.

Cooper JA. 2008. A mechanism for inside-out lamination in the neocortex. Trends Neurosci. 31:113–119.

D'Arcangelo G, Miao GG, Chen SC, Soares HD, Morgan JI, Curran T. 1995. A protein related to extracellular matrix proteins deleted in the mouse mutant reeler. Nature. 374:719–723.

DeArmond SJ, Eng LF, Rubinstein LJ. 1980. The application of glial fibrillary acidic (GFA) protein immunohistochemistry in neurooncology. Pathol Res Pract. 68:374–394.

Dulabon L, Olson EC, Taglienti MG, Eisenhuth S, McGrath B, Walsh CA, Kreidberg JA, Anton ES. 2000. Reelin binds alpha3beta1 integrin and inhibits neuronal migration. Neuron. 27:33–44.

Elias LA, Wang DD, Kriegstein AR. 2007. Gap junction adhesion is necessary for radial migration in the neocortex. Nature. 448:901–907.

Feng L, Allen NS, Simo S, Cooper JA. 2007. Cullin 5 regulates Dab1 protein levels and neuron positioning during cortical development. Genes Dev. 21:2717–2730.

Franco SJ, Martinez-Garay I, Gil-Sanz C, Harkins-Perry SR, Muller U. 2011. Reelin regulates cadherin function via Dab1/Rap1 to control neuronal migration and lamination in the neocortex. Neuron. 69:482–497.

Gonda Y, Sakurai H, Hirata Y, Tabata H, Ajioka I, Nakajima K. 2007. Expression profiles of insulin-like growth factor binding protein-like 1 in the developing mouse forebrain. Gene Expr Patterns. 7:431–440.

Gongidi V, Ring C, Moody M, Brekken R, Sage EH, Rakic P, Anton ES. 2004. SPARC-like 1 regulates the terminal phase of radial glia-guided migration in the cerebral cortex. Neuron. 41:57–69.

Gupta A, Tsai LH, Wynshaw-Boris A. 2002. Life is a journey: a genetic look at neocortical development. Nat Rev Genet. 3:342–355.

Hack I, Hellwig S, Junghans D, Brunne B, Bock HH, Zhao S, Frotscher M. 2007. Divergent roles of ApoER2 and Vldlr in the migration of cortical neurons. Development. 134:3883–3891.

Hashimoto-Torii K, Torii M, Sarkisian MR, Bartley CM, Shen J, Radtke F, Gridley T, Sestan N, Rakic P. 2008. Interaction between Reelin and Notch signaling regulates neuronal migration in the cerebral cortex. Neuron. 60:273–284.

Hatanaka Y, Hisanaga S, Heizmann CW, Murakami F. 2004. Distinct migratory behavior of early- and late-born neurons derived from the cortical ventricular zone. J Comp Neurol. 479:1–14.

Hernandez-Miranda LR, Cariboni A, Faux C, Ruhrberg C, Cho JH, Cloutier JF, Eickholt BJ, Parnavelas JG, Andrews WD. 2011. Robo1 regulates semaphorin signaling to guide the migration of cortical interneurons through the ventral forebrain. J Neurosci. 31:6174–6187.

Honda T, Kobayashi K, Mikoshiba K, Nakajima K. 2011. Regulation of cortical neuron migration by the Reelin signaling pathway. Neurochem Res. 36:1270–1279.

Howell BW, Hawkes R, Soriano P, Cooper JA. 1997. Neuronal position in the developing brain is regulated by mouse disabled-1. Nature. 389:733–737.

Huang Z. 2009. Molecular regulation of neuronal migration during neocortical development. Mol Cell Neurosci. 42:11–22.

Kidd T, Brose K, Mitchell KJ, Fetter RD, Tessier-Lavigne M, Goodman CS, Tear G. 1998. Roundabout controls axon crossing of the CNS midline and defines a novel subfamily of evolutionarily conserved guidance receptors. Cell. 92:205–215.

Kidd T, Russell C, Goodman CS, Tear G. 1998. Dosage-sensitive and complementary functions of roundabout and commissureless control axon crossing of the CNS midline. Neuron. 20:25–33.

Kubo K, Honda T, Tomita K, Sekine K, Ishii K, Uto A, Kobayashi K, Tabata H, Nakajima K. 2010. Ectopic Reelin induces neuronal aggregation with a normal birthdate-dependent "inside-out" alignment in the developing neocortex. J Neurosci. 30:10953–10966.

López-Bendito G, Flames N, Ma L, Fouquet C, Di Meglio T, Chedotal A, Tessier-Lavigne M, Marín O. 2007. Robo1 and Robo2 cooperate to control the guidance of major axonal tracts in the mammalian forebrain. J Neurosci. 27:3395–3407.

Magdaleno S, Keshvara L, Curran T. 2002. Rescue of ataxia and preplate splitting by ectopic expression of Reelin in reeler mice. Neuron. 33:573–586.

McConnell SK, Kaznowski CE. 1991. Cell cycle dependence of laminar determination in developing neocortex. Science. 254:282–285.

Moers A, Nurnberg A, Goebbels S, Wettschureck N, Offermanns S. 2008. Galpha12/Galpha13 deficiency causes localized overmigration of neurons in the developing cerebral and cerebellar cortices. Mol Cell Biol. 28:1480–1488.

Nadarajah B, Brunstrom JE, Grutzendler J, Wong RO, Pearlman AL. 2001. Two modes of radial migration in early development of the cerebral cortex. Nat Neurosci. 4:143–150.

Nadarajah B, Parnavelas JG. 2002. Modes of neuronal migration in the developing cerebral cortex. Nat Rev Neurosci. 3:423–432.

Namba T, Maekawa M, Yuasa S, Kohsaka S, Uchino S. 2009. The Alzheimer's disease drug memantine increases the number of radial glial-like progenitor cells in adult hippocampus. Glia. 75:1082–1090.

Nichols AJ, Olson EC. 2010. Reelin promotes neuronal orientation and dendritogenesis during preplate splitting. Cereb Cortex. 20:2213–2223.
Nieto M, Monuki ES, Tang H, Imitola J, Haubst N, Khoury SJ, Cunningham J, Gotz M, Walsh CA. 2004. Expression of Cux-1 and Cux-2 in the subventricular zone and upper layers II-IV of the cerebral cortex. J Comp Neurol. 479:168–180.
Niwa H, Yamamura K, Miyazaki J. 1991. Efficient selection for high-expression transfectants with a novel eukaryotic vector. Gene. 108:193–199.
Noctor SC, Martinez-Cerdeno V, Ivic L, Kriegstein AR. 2004. Cortical neurons arise in symmetric and asymmetric division zones and migrate through specific phases. Nat Neurosci. 7:136–144.
Ogawa M, Miyata T, Nakajima K, Yagyu K, Seike M, Ikenaka K, Yamamoto H, Mikoshiba K. 1995. The reeler gene-associated antigen on Cajal-Retzius neurons is a crucial molecule for laminar organization of cortical neurons. Neuron. 14:899–912.
Olson EC, Kim S, Walsh CA. 2006. Impaired neuronal positioning and dendritogenesis in the neocortex after cell-autonomous Dab1 suppression. J Neurosci. 26:1767–1775.
O'Rourke NA, Dailey ME, Smith SJ, McConnell SK. 1992. Diverse migratory pathways in the developing cerebral cortex. Science. 258:299–302.
Pearlman AL, Faust PL, Hatten ME, Brunstrom JE. 1998. New directions for neuronal migration. Curr Opin Neurobiol. 8:45–54.
Pinto-Lord MC, Evrard P, Caviness VS, Jr. 1982. Obstructed neuronal migration along radial glial fibers in the neocortex of the reeler mouse: a Golgi-EM analysis. Brain Res. 256:379–393.
Rakic P. 1972. Mode of cell migration to the superficial layers of fetal monkey neocortex. J Comp Neurol. 145:61–83.
Rakic P. 1974. Neurons in rhesus monkey visual cortex: systematic relation between time of origin and eventual disposition. Science. 183:425–427.
Rhee J, Buchan T, Zukerberg L, Lilien J, Balsamo J. 2007. Cables links Robo-bound Abl kinase to N-cadherin-bound beta-catenin to mediate Slit induced modulation of adhesion and transcription. Nat Cell Biol. 9:883–892.
Rhee JR, Mahfooz NS, Arregui C, Lilien J, Balsamo J, VanBerkum MFA. 2002. Activation of the repulsive receptor Roundabout inhibits N-cadherin-mediated cell adhesion. Nat Cell Biol. 4:798–805.
Sanada K, Gupta A, Tsai LH. 2004. Disabled-1-regulated adhesion of migrating neurons to radial glial fiber contributes to neuronal positioning during early corticogenesis. Neuron. 42:197–211.
Sekine K, Honda T, Kawauchi T, Kubo K, Nakajima K. 2011. The outermost region of the developing cortical plate is crucial for both the switch of the radial migration mode and the dab1-dependent "inside-out" lamination in the neocortex. J Neurosci. 31:9426–9439.
Sheldon M, Rice DS, D'Arcangelo G, Yoneshima H, Nakajima K, Mikoshiba K, Howell BW, Cooper JA, Goldowitz D, Curran T. 1997. Scrambler and yotari disrupt the disabled gene and produce a reeler-like phenotype in mice. Nature. 389:730–733.
Tabata H, Kanatani S, Nakajima K. 2009. Differences of migratory behavior between direct progeny of apical progenitors and basal progenitors in the developing cerebral cortex. Cereb Cortex. 19:2092–2105.
Tabata H, Nakajima K. 2001. Efficient *in utero* gene transfer system to the developing mouse brain using electroporation: visualization of neuronal migration in the developing cortex. Neuroscience. 103:865–872.
Tabata H, Nakajima K. 2003. Multipolar migration: the third mode of radial neuronal migration in the developing cerebral cortex. J Neurosci. 23:9996–10001.
Takahashi T, Goto T, Miyama S, Nowakowski RS, Caviness VS, Jr. 1999. Sequence of neuron origin and neocortical laminar fate: relation to cell cycle of origin in the developing murine cerebral wall. J Neurosci. 19:10357–10371.
Teng J, Takei Y, Harada A, Nakata T, Chen J, Hirokawa N. 2001. Synergistic effects of MAP2 and MAP1B knockout in neuronal migration, dendritic outgrowth, and microtubule organization. J Cell Biol. 155:65–76.
Trommsdorff M, Gotthardt M, Hiesberger T, Shelton J, Stockinger W, Nimpf J, Hammer RE, Richardson JA, Herz J. 1999. Reeler/disabled-like disruption of neuronal migration in knockout mice lacking the VLDL receptor and ApoE receptor 2. Cell. 97:689–701.
Tsai LH, Gleeson JG. 2005. Nucleokinesis in neuronal migration. Neuron. 46:383–388.
Walsh CA, Goffinet AM. 2000. Potential mechanisms of mutations that affect neuronal migration in man and mouse. Curr Opin Genet Dev. 10:270–274.
Yano M, Hayakawa-Yano Y, Mele A, Darnell RB. 2010. Nova2 regulates neuronal migration through an RNA switch in disabled-1 signaling. Neuron. 66:848–858.
Yoshida M, Assimacopoulos S, Jones KR, Grove EA. 2006. Massive loss of Cajal-Retzius cells does not disrupt neocortical layer order. Development. 133:537–545.
Zheng W, Geng AQ, Li PF, Wang Y, Yuan XB. 2011. Robo4 regulates the radial migration of newborn neurons in developing neocortex. Cereb Cortex. (in press).

BRAIN RESEARCH 1507 (2013) 35–44

Available online at www.sciencedirect.com

SciVerse ScienceDirect

www.elsevier.com/locate/brainres

Brain Research

Research Report

Functional down-regulation of axotomized rat facial motoneurons

Toshihumi Ichimiya[a], *Shinichi Yamamoto*[a], *Yoshinaru Honda*[a], *Reika Kikuchi*[a], *Shinichi Kohsaka*[b], *Kazuyuki Nakajima*[a,b,*]

[a]*Department of Bioinformatics, Faculty of Engineering, Soka University, Tokyo 192-8577, Japan*
[b]*Department of Neurochemistry, National Institute of Neuroscience, Tokyo 187-8502, Japan*

ARTICLE INFO

Article history:
Accepted 23 February 2013
Available online 28 February 2013

Keywords:
Transection
Facial motoneuron
Choline acetyltransferase
Vesicular acetylcholine transporter
Acetylcholine receptor

ABSTRACT

Functional alterations in injured motoneurons were quantitatively analyzed in axotomized rat facial nuclei. Choline acetyltransferase (ChAT), vesicular acetylcholine transporter (VAchT) and m2 muscarinic acetylcholine receptor (m2MAchR) were chosen as indicators of motoneuron function. Immunoblotting showed that the amounts of ChAT in the ipsilateral facial nucleus significantly decreased to below 20% from 3 to 14 days after transection. The decreased level of ChAT in injured motoneurons was ascertained by immunohistochemical study. However, at 4–5 weeks after transection the level of ChAT was restored to that of control side. The amounts of VAchT in the transected nucleus were observed to decrease to below 20% in the first 14 days after transection. The down-regulated levels of VAchT in injured motoneurons were confirmed by immunohistochemical results. The reduced VAchT levels returned to the control levels at 4–5 weeks following insult. The level of m2MAchR in the ipsilateral nucleus was recognized to decrease to below 10% starting on the 5th day after insult, and the low levels were sustained for 5 weeks. Nissl staining at 5 days and 12 days after insult revealed that facial motoneurons in the transected nucleus were almost all alive. Altogether, these results indicate that transected adult rat facial motoneurons are functionally depressed with down-regulated levels of ChAT, VAchT and m2MAchR during the first 14 days after insult, and during Weeks 4–5 ChAT and VAchT levels are restored while the levels of m2MAchR remain low.

Abbreviations: ABC, avidin–biotin–peroxidase complex; cFms, receptor for M-CSF; ChAT, choline acetyltransferase; HRP, horseradish peroxidase; Iba1, ionized Ca^{2+} binding adapter molecule 1; M-CSF, macrophage colony stimulating factor; m2MAchR, m2 muscarinic acetylcholine receptor; NR3B, NMDA receptor 3B subunit; PAGE, polyacrylamide gel electrophoresis; PBS, phosphate buffered solution; SDS, sodium dodecyl sulfate; VAchT, vesicular acetylcholine transporter

*Corresponding author at: Soka University Department of Bioinformatics Faculty of Engineering Institute of Life Science -236, Tangi-machi, Hachioji, Tokyo 192-8577, Japan. Fax: +81 426 91 9312.
E-mail address: nakajima@t.soka.ac.jp (K. Nakajima).

0006-8993/$ - see front matter © 2013 Elsevier B.V. All rights reserved.
http://dx.doi.org/10.1016/j.brainres.2013.02.044

1. Introduction

It has been traditionally recognized that the transection of facial nerves in adult rats results in retrograde injury to the motoneurons (Kreutzberg, 1996). Soon after injury, the motoneurons change their expressions of genes such as c-jun and Jun-B (Haas et al., 1993). Subsequently, such rats undergo changes in cytoskeletal molecules, metabolic enzymes, neuropeptides and cytokines (Moran and Graeber, 2004). Accompanying these changes, motoneuron function-related proteins such as acetylcholinesterase (Tetzlaff and Kreutzberg, 1984), vesicular acetylcholine transporter (VAchT) and muscarinic receptors (Hoover and Hancock, 1985) also decline. However, the definitive method for evaluating the process of injury/degeneration of motoneurons following facial nerve insult, a quantitative time-course analysis, has not fully been carried out.

Facial motoneurons exist in the nucleus of the brainstem, and they extend axons to the facial expression muscles through the cranial bone. Transection of the facial nerve fibers at the stylomastoid foramen can cause insult to the motoneurons in the ipsilateral nucleus (Graeber et al., 1998). The superiority of this injury model is that the blood–brain barrier in the ipsilateral facial nucleus is sustained as normal, and blood-derived cells and constituents do not infiltrate the parenchyma (Moran and Graeber, 2004).

Thus, using the rat facial-nerve-transection model, we analyzed quantitatively the functional changes of injured motoneurons in the course of time after facial nerve insult. As indicators for motoneuronal function, we selected choline acetyltransferase (ChAT), which synthesizes acetylcholine from acetyl CoA and choline (Hersh, 1982; Engel et al., 2003), and VAchT, which packs the acetylcholine into the synaptic vesicles (Eiden, 1998; Yao and Godfrey, 1999). The m2 muscarinic acetylcholine receptor (m2MAchR) has also been identified as a motoneuronal indicator (Hoover et al.,1996; Brown, 2010).

Since the levels of ChAT, VAchT and m2MAchR in the transected facial nucleus were speculated to change at an early time after injury, initially we investigated the temporary changes focusing on a period of 1–14 days following insult. Expecting the functional recovery of injured motoneurons at a later time post-insult, we evaluated the indicators at 3, 4 and 5 weeks after axotomy.

2. Results

2.1. *Changes in levels of choline acetyltransferase*

Each set of facial nuclei recovered at 1, 3, 5, 7, and 14 days after transection was analyzed for ChAT by immunoblotting. The results revealed that the amounts of ChAT in the ipsilateral nucleus significantly decreased at 3, 5, 7 and 14 days after transection compared to those of the contralateral nucleus (Fig. 1A, ChAT). This profile was different from that of the microglial marker, ionized Ca^{2+} binding adapter molecule 1 (Iba1), whose levels were up-regulated in the ipsilateral nucleus from Days 3–14 after transection (Fig. 1A, Iba1). The upregulation of Iba1 in the ipsilateral nucleus is ascribed to the presence of activated/proliferating microglia (Yamamoto et al., 2010). Quantification of ChAT in immunoblotting analysis indicated an approximately 80% decrease of the total ChAT in the injured nucleus at 3 days, and an 80–90% decrease of the total amounts within 5–14 days after injury (Fig. 1B).

Avidin–biotin–peroxidase complex (ABC) immunohistochemical methods confirmed the above immunoblotting results. Many motoneurons were strongly stained with anti-ChAT antibody in the control facial nucleus at 5 days after injury (Fig. 1C, Ct), whereas only weakly stained cells were observed in the ipsilateral nucleus (Fig. 1C, Op).

In the magnified image from fluorescence staining, a number of positive granules were recognized in motoneuron-like cells in the control nucleus (Fig. 1D, Ct), while in the ipsilateral nucleus lesser granules were sparsely seen in the ipsilateral nucleus (Fig. 1D, Op).

To ascertain whether anti-ChAT antibody-positive cells are motoneurons, the control facial nucleus was dually stained with anti-ChAT antibody and anti-NMDA receptor 3B subunit (NR3B) antibody (a marker of motoneurons; Matsuda et al., 2003). The results showed that ChAT and NR3B were almost co-localized (Fig. 1E), indicating that the anti-ChAT antibody-stained cells were motoneurons. Therefore, these results indicated that the expression of ChAT proteins in motoneurons is down-regulated after nerve injury.

2.2. *Changes in the levels of vesicular acetylcholine transporter*

Changes of VAchT in the ipsilateral facial nucleus were examined during Days 1–14 post-insult. The amounts of VAchT in the injured nucleus were observed to decline from Days 1 to 14 after injury (Fig. 2A). The quantification of the results of immunoblotting indicated that the levels of VAchT in the transected nucleus decreased to 2–6% of the control amounts during Days 3–14 after insult (Fig. 2B). In the immunohistochemical study, the motoneurons in the control nucleus were widely stained with anti-VAchT antibody (Fig. 2C, upper panels, Ct), but only weakly stained cells were seen on the ipsilateral side (Fig. 2C, upper panels, Op). The magnified images indicating that the number of vesicles stained with anti-VAchT antibody was lower in the injured motoneurons (Fig. 2C, lower panels, Ct vs. Op). Since the vesicles are distributed mainly at the periphery of motoneuron cell bodies (Fig. 2C, lower panels, Ct), the outer regions of soma appear to be strongly stained by anti-VAchT antibody. Similar localization of VAchT in facial motoneurons has been reported by Gilmor et al. (1996). Thus, these results (Fig. 2A–C) indicate that the amount of VAchT in the vesicles is down-regulated in the injured motoneurons.

2.3. *Changes in the levels of muscarinic acetylcholine receptor*

The influence of nerve transection on the level of acetylcholine receptors in the ipsilateral facial nucleus was investigated. As a metabotropic-type acetylcholine receptor, m2MAchR was selected, because this receptor type is extensively expressed in the peripheral nervous system including the facial motonucleus.

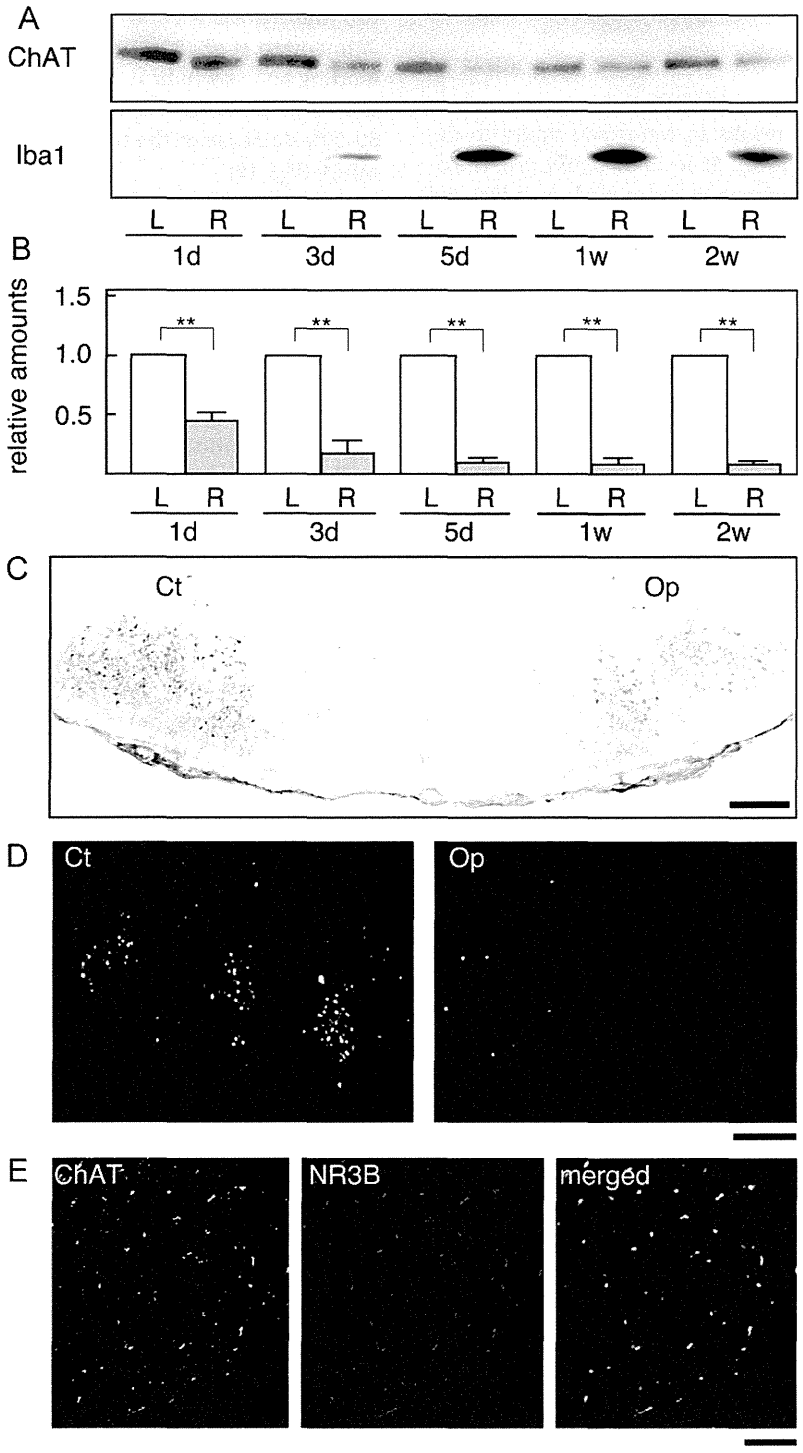

Fig. 1 – Determination of ChAT in transected facial nucleus. Sets of contralateral (Left side; L) and ipsilateral (Right side; R) facial nuclei recovered at 1, 3, 5, 7 and 14 days after transection were immunoblotted for choline acetyltransferase (ChAT) and ionized Ca^{2+} binding adapter molecule 1 (Iba1) (A). The intensity of the ChAT bands in A was determined by a densitometer, and the value of the transected facial nucleus (R) was expressed as the value relative to that of the control nucleus (L). The data shown are means ± SDs from four independent experiments (*$P<0.05$, **$P<0.01$) (B). Brainstem sections obtained at 5 days after transection were immunohistochemically stained with anti-ChAT antibody according to the ABC method (C). A control nucleus (Ct) and injured nucleus (Op) are shown on the left and right sides, respectively. Scale bar = 400 μm. The same brainstem sections were stained with anti-ChAT antibody according to the fluorescence method. ChAT was visualized by Alexa Fluor 488 (green). Control (Ct) and transected (Op) sides are shown on the left and right, respectively (D). Scale bar = 30 μmm. The same brainstem sections were dually stained with anti-ChAT antibody and NMDA receptor 3B subunit (NR3B) antibody according to fluorescence methods. In the control facial nucleus, ChAT-positive cells (ChAT) and NR3B-positive cells (NR3B) were visualized by Alexa Fluor-488 (green) and Alexa Fluor-568 (red), respectively. The merged image is shown on the right-hand side (E). Scale bar = 200 μmm.

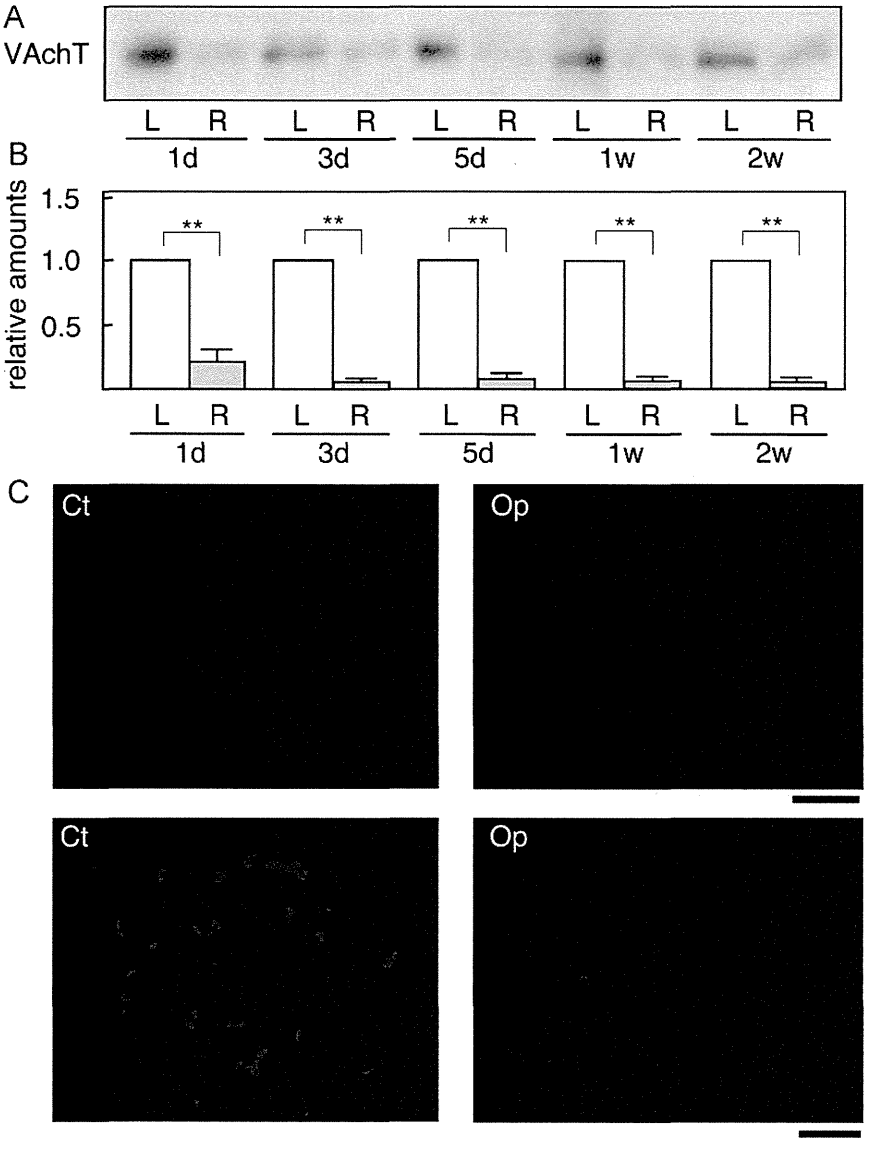

Fig. 2 – Determination of VAChT in transected facial nucleus. Sets of contralateral (L) and ipsilateral (R) facial nuclei recovered at 1, 3, 5, 7 and 14 days after transection were immunoblotted for vesicular acetylcholine transporter (VAchT) (A). The intensity of the VAchT bands in A was determined by densitometer, and was expressed as the value of the transected facial nucleus (R) relative to that of the control nucleus (L). Data shown are means ± SDs from three independent experiments. ($^{*}P<0.05$, $^{**}P<0.01$) (B). Brainstem sections obtained at 5 days after transection were immunohistochemically stained with anti-VAchT antibody according to the fluorescence method. VAchT was visualized by Alexa Fluor 568 (red). Control (Ct) and transected (Op) sides are shown at left and right, respectively (C, upper panels). Scale bar = 100 μmm. Respective magnified images are shown in the lower panels. Scale bar = 10 μmm.

In the time-course experiment, the levels of m2MAchR in the transected facial nucleus severely decreased after 5 days, and the low levels lasted over 14 days (Fig. 3A). The quantified results signified that the amounts of m2MAchR are kept at 82–98% for the 1–3 days after insult, and thereafter fall to 4–6% (Fig. 3B). The decreased level of m2MAchR in the injured nucleus was confirmed by immunohistochemical study (Fig. 3C), showing that the number of anti-m2MAchR antibody-positive cells largely fell in the ipsilateral nucleus (Fig. 3C, Ct vs. Op).

Comparing the results of Figs. 1A and 3A, the reduction of m2MAchR in the ipsilateral nucleus appeared to occur slightly after that of ChAT. The levels of ChAT began to decrease from Day 3 after nerve injury (Fig. 1A), but those of m2MAchR began to decrease from 5 days after injury (Fig. 3A). Thus, we tried to confirm immunohistochemically the delayed response of m2MAchR in brainstem sections prepared at 3 days after transection (Fig. 4). The results showed that the injured motoneurons had significantly reduced ChAT levels (Fig. 4A, upper panels, Ct vs. Op), while they retained close to normal levels of m2MAchR (Fig. 4A, lower panels, Ct vs. Op).

In addition, the localization of ChAT and m2MAchR in the control nucleus was examined. The dual staining with anti-ChAT antibody and anti-m2MAchR antibody indicated that